JOURNAL OF GEOPHYSICAL RESEARCH, VOL. 103, NO. C4, PAGES 7807–7831, APRIL 15, 1998

VIERS-1 scatterometer model

P. A. E. M. Janssen,[1] H. Wallbrink, C. J. Calkoen,[2] D. van Halsema,[3]
W. A. Oost, and P. Snoeij[4]

Department of Oceanography, Royal Netherlands Meteorological Institute, De Bilt, Netherlands

Abstract. In this paper a description is given of a physically based theoretical ocean backscatter model (called the VIERS-1 model) for intermediate incidence angles, and a comparison of its performance against the CMOD4 empirical model is made. The VIERS-1 scatterometer algorithm is based on a two-scale composite surface model which includes both specular and Bragg scattering. Its short wave model is based on the energy balance equation and accounts for viscous damping, slicks, dissipation due to whitecapping, and nonlinear three- and four-wave interactions. A number of parameters in the model have been determined by means of laboratory data and analyzed European Centre for Medium-Range Weather Forecasts (ECMWF) winds. Because of the two-scale approach the wave number up to which Bragg scattering applies should be determined. This is done by means of laboratory data at X band. In addition, laboratory data of the wave spectrum have been utilized to validate the VIERS-1 short wave spectrum. An inverse of the algorithm is developed to derive wind speed and direction from the observed (ERS-1) backscatter and by comparison with ECMWF analyzed winds' three parameters for the short wave spectrum, namely, the Phillips parameter, the directional width of the spectrum, and the wave number boundary between gravity waves and short waves have been obtained. Comparisons between VIERS-1, C band model, version 4 (CMOD4), and ECMWF analyses are made. VIERS-1 performs better in the high wind speed range, and this feature is of importance when scatterometer winds are assimilated into an atmospheric model. However, in terms of backscatter rather than wind speed, CMOD4 shows better results. It is suggested that this is caused by the too simple directional distribution of the VIERS-1 short wave spectrum.

1. Introduction

Traditionally, the operational retrieval algorithms for the scatterometer, which relate the radar backscatter measurements to the surface wind vectors, have been empirical. A review of the history of this empirical relationship is given by, for example, *Moore and Fung* [1979], *Jones et al.* [1982], *Schroeder et al.* [1982], and *Barrick and Swift* [1980]. After *Moore and Pierson* [1967] proposed to use a satellite scatterometer's radar echo to determine the wind speed at sea, a variety of early scatterometer models appeared in the 1970s [e.g., *Valenzuela et al.*, 1971; *Guinard et al.*, 1971; *Jones et al.*, 1977; *Moore and Fung*, 1979; *Wentz et al.*, 1984]. The most successful scatterometer model of the early 1980s was the Seasat A scatterometer system (SASS 1) model. The SASS 1 model assumed a power law between the radar backscatter σ and wind speed U and was tuned to a subset of the available surface truth wind data from the Joint Air-Sea Interaction Experiment (JASIN). The wind speed data set was relatively small, 4–16 m/s. When results of the tuned SASS 1 model were compared with the JASIN data not used in the tuning, a favorable agreement was found, giving confidence in the empirical approach. Nevertheless, *Woiceshyn et al.* [1986] and *Anderson et al.* [1987] pointed out several weak points of the SASS 1 algorithm. First of all, low wind speeds were systematically too high while high wind speeds were too low. Secondly, winds obtained from horizontal polarization were not consistent with vertical polarization, suggesting that a power law relationship between backscatter and wind is not adequate. Furthermore, it was also felt that other geophysical parameters such as atmospheric stability and water viscosity would have resulted in an improved wind field retrieval, in particular at the lower wind speeds.

Despite the shortcomings, the statistical fitting approach has resulted in a useful algorithm as follows from the work of *Stoffelen and Anderson* [1997], although a somewhat more sophisticated power law relationship needed to be introduced. The resulting backscatter algorithm, C band model, version 4 (CMOD4), showed a very good fit in backscatter space while in comparison with European Centre for Medium-Range Weather Forecasts (ECMWF) wind fields, the retrieved wind velocity had a small wind speed error of about 2 m/s and directional error of the order of 20–30°. However, CMOD4 showed for low and high wind speed similar problems as the SASS 1 algorithm. When using CMOD4 in ECMWF's analysis system, *Gaffard and Roquet* [1995] found that the underestimation of wind speed in the high wind speed range resulted in less deep lows (by as much as 8 hPa) and, as a consequence, the quality of the atmospheric forecast suffered. By applying a wind speed dependent bias correction to CMOD4 (which was

[1]Now at European Centre for Medium-Range Weather Forecasts, Reading, England, United Kingdom.
[2]Now at Advisory and Research Group on Geo Observation Systems and Services, Vollenhove, Netherlands.
[3]Now at Physics and Electronics Laboratory, Netherlands Organization for Applied Scientific Research, Delft.
[4]Now at Delft University of Technology, Delft, Netherlands.

Paper number 97JC02911.
0148-0227/98/97JC-02911$09.00

obtained by a comparison with buoy wind speed data) the scatterometer winds were found to have a favorable impact on atmospheric analysis and forecast and even on the ocean wave analysis and forecast [*Andersson et al.*, 1998].

From a scientific point of view the assumption that the backscatter only depends on the local wind field may be questioned, however, since the backscatter reflects to some extent the state of the high-frequency wind waves. The spectrum of wind-generated gravity-capillary waves not only depends on the local wind but is determined by a number of physical processes, namely, wind input, nonlinear three- and four-wave interaction, viscous dissipation, and dissipation due to slicks. Thus, when the waves are sufficiently steep, which may occur, for example, for young wind seas, nonlinear processes may be dominant so that the state of the short waves is, through the energy cascade, mainly determined by the longer gravity waves. The state of the longer waves depends on factors such as coastal geometry, duration of a storm system, currents, and bathymetry, and therefore the radar backscatter may depend on these environmental circumstances as well. On the other hand, for low wind speed, viscous dissipation and dissipation due to slicks may be relevant processes in determining the shape of the short wave spectrum, again suggesting that not only the local wind determines the backscatter. Furthermore, it should be pointed out that the radar backscatter shows an additional dependence on the state of the long gravity waves because the short waves which provide the backscatter are tilted by the longer gravity waves. This effect is especially relevant for small incidence angles.

The above considerations prompted an extensive investigation into the dependence of the radar backscatter on physical parameters such as wind speed, sea state, the presence of slicks, and the air-sea temperature difference. The work was supported by the Netherlands Remote Sensing Board (BCRS), and the Verification and Interpretation of ERS (VIERS) group emerged, which started an experimental study in the laboratory and at sea to address the above mentioned issues. The radar used in these studies operated at X band. Parallel to the experimental work, the VIERS group started the development of a scatterometer algorithm based on the present understanding of the radar backscatter process and of the relevant processes governing the shape of the gravity-capillary spectrum. The observed results on radar backscatter and the short wave spectrum were used as a guideline to tune a number of unknown parameters in the scatterometer algorithm. As a result, a backscatter algorithm based on physics rather than empirical fitting was obtained [*van Halsema et al.*, 1989; *Calkoen et al.*, 1990; *Snoeij et al.*, 1993; *Janssen et al.*, 1995].

Confidence in the performance of the VIERS algorithm increased when the simulated backscatter, obtained using the ECMWF wind and wave model (WAM) wave fields, was compared with the backscatter as observed by the ERS-1 satellite. The air-sea temperature difference was set to zero since neutral stability is the most common situation that occurs over the oceans. The period of interest was November 6, 1991, at 1200 UT. In Figure 1 we compare the simulated backscatter with the observed ones showing an overall good agreement, even for low wind speed. As a benchmark, we have also shown results of the present operational scatterometer algorithm CMOD4. We conclude from this comparison that the VIERS scatterometer algorithm performs well, even compared to CMOD4. We add to this that while the VIERS-1 two-scale composite surface model was tuned at X band, the ERS-1 satellite operates at C band, thus giving some confidence in the validity of the VIERS-1 model over a wider range of radar frequencies. Despite the good agreement between observed and simulated backscatter, it should be pointed out that the root-mean-square (rms) error, which is of the order of 2–3 dB, is large when compared with the observation error, which is about 0.2 dB. This could imply two things. On the one hand, it can be argued that the large rms error is caused by model errors. This possibility seems unlikely, however, since it is known that CMOD4, which has the bigger rms error, has a reasonable skill in retrieving wind speed and direction. On the other hand, a source of error could be provided by the analyzed wind and wave field used in the generation of the simulated backscatter with the scatterometer algorithms. Hence the observed backscatter might contain relevant information regarding, for example, the surface wind field. In view of the large difference between the rms error of Figure 1 and the measurement error the information contained in the observed backscatter might therefore be quite considerable. In order to investigate this we need to invert the VIERS algorithm so that a retrieval of wind speed and direction from the observed backscatter becomes feasible.

The program of this paper is as follows. In section 2 a review of the VIERS scatterometer algorithm is given, including a description of the energy balance of short waves. Once the wave spectrum is known, a two-scale model is used to determine the normalized backscatter. The scatterometer algorithm thus obtained gives the radar backscatter as the function of a number of geophysical parameters such as wind speed and direction, the sea state, slicks, air-sea stability, the sea surface temperature, and, of course, geometrical parameters such as the look angle and the incidence angle. For practical application discussed in this paper we restrict our attention to the usual parameters, wind speed and direction and incidence angle, and allow the sea state as an additional parameter. Effects of air-sea stability are disregarded because, except near coasts, the stability of the atmosphere over the oceans is almost always close to neutral and only an averaged effect of slicks is taken into account. Nevertheless, the VIERS algorithm is computationally very expensive and is as such not a feasible option when used in routine applications such as wind retrieval for determining the analyzed weather over the oceans.

For practical applications we therefore generated tabulated values of the normalized radar backscatter σ_0 as a function of wind speed, wind direction, incidence angle, and sea state. Once this table of σ_0 is known, we retrieve wind speed and direction from the observed ERS-1 σ_0 triplet by minimizing a measure of distance between observed and modeled backscatter under the side constraint that the retrieved wind direction does not deviate too much from the wind direction provided by the ECMWF model. This procedure allows for a unique solution of the wind vector and is discussed in section 3.

Retrieved wind vectors by means of the VIERS scatterometer algorithm are compared in section 4 with the ECMWF analyzed wind fields, and it is found that VIERS and ECMWF winds are compatible in a statistical sense. As a reference, we use results from CMOD4. A direct comparison between VIERS and CMOD4 winds reveals a good agreement between the two products, except that in the high wind speed range, VIERS has higher winds than CMOD4, while at low winds, VIERS has lower winds. In view of the problems CMOD4 has at the extreme wind speed ranges (which, as *Gaffard and Roquet* [1995] have pointed out, have a detrimental impact on the forecast) it is concluded that the VIERS model is performing

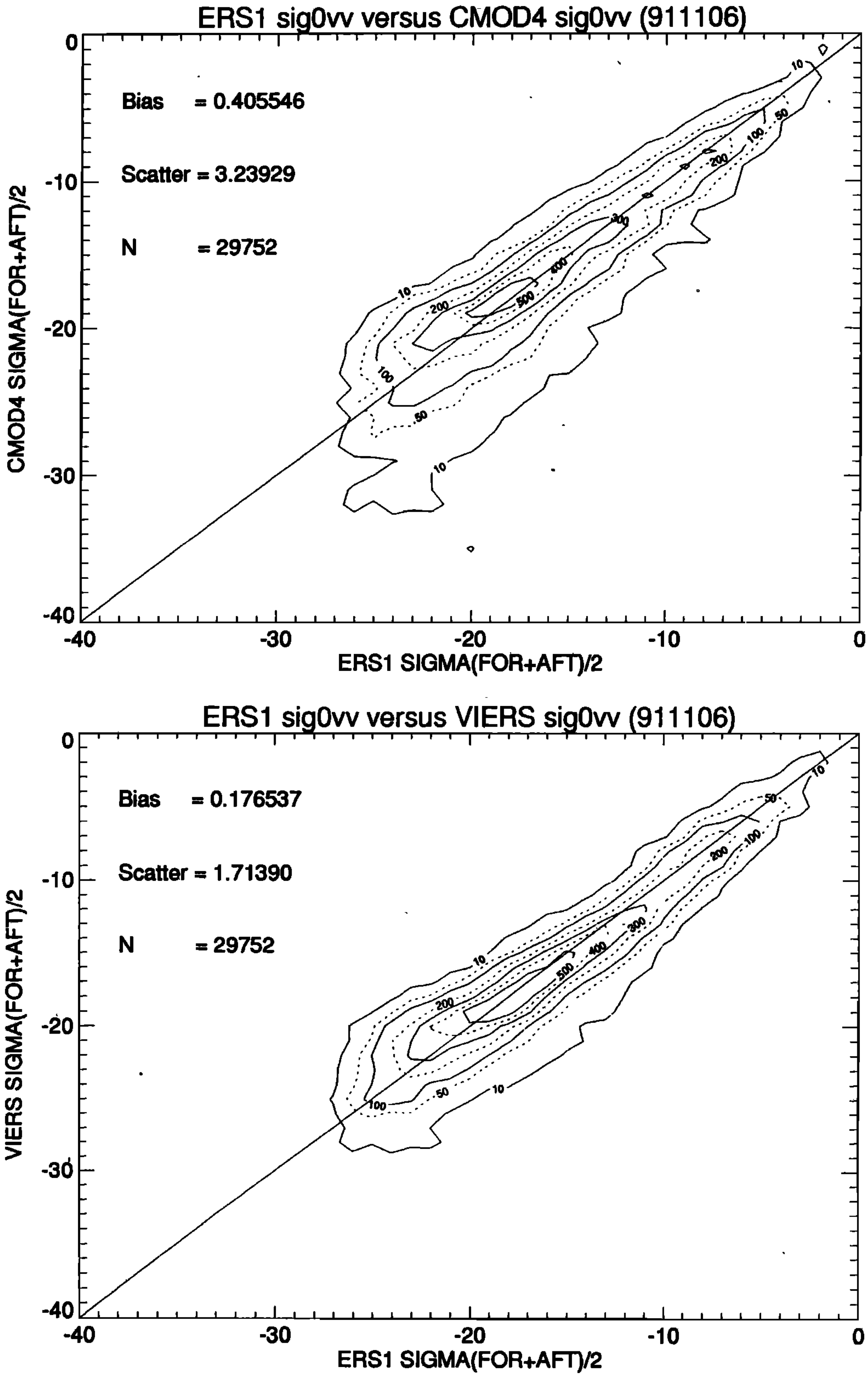

Figure 1. Simulated normalized backscatter using (top) CMOD4 and (bottom) VIERS algorithm versus observed backscatter from ERS-1 on November 6, 1991.

better. Nevertheless, it should be emphasized that the misfit in σ_0 space between modeled and observed backscatter is generally larger for VIERS than for CMOD4. This is probably caused by a too simple directional distribution of wind waves in VIERS. After the statistical comparison we proceed with a synoptic discussion of the differences between retrieved and analyzed wind concentrating on a frontal system that occurred in the Norwegian Sea on November 6, 1991. A summary of conclusions is presented in section 5, and suggestions for improvements are given as well.

2. Viers Model

To our knowledge to date, the most successful modeling attempt of the scattering of the radar signal at the sea surface is due to *Donelan and Pierson* [1987]. These authors obtained the spectrum of gravity-capillary waves from a simplified energy balance, consisting of wind input and dissipation through viscosity and wave breaking. Combining this short wave number with the observed directional spectra of *Donelan et al.* [1985], the complete surface wave spectrum is then known.

Scattering off a surface with a broad spectrum of waves is reasonably well modeled by means of a so-called two-scale approach [*Valenzuela*, 1978; *Plant*, 1990]. Thus the normalized radar backscatter can be found by integrating the scatter from the individual facets (which are tilted by the longer gravity waves) weighted with the probability that the water surface is tilted by a certain angle. Introducing a separation scale wave number k_c, for high wave numbers ($k > k_c$) the main scattering mechanism is assumed to be Bragg scattering, while for $k < k_c$, specular reflection is taken. Results are fairly weakly dependent on the choice of k_c [*Plant*, 1990]; *Donelan and Pierson* [1987] selected $k_c = k_b/40$, where k_b is the Bragg wave number

$$k_b = 2k_R \sin \theta_l \tag{1}$$

where θ_l is the local incidence angle, which depends on the tilt of the water surface by the long waves, and k_R is the radar wave number.

Application of the *Donelan and Pierson* [1987] scatterometer algorithm to the VIERS wave tank data set revealed a number of shortcomings in the model [*Calkoen et al.*, 1990]. First of all, considerable discrepancies between modeled and observed short wave spectral shape were found; for large winds the modeled spectrum drops off too rapidly, while at low wind speed, considerable amounts of wave energy were observed beyond the viscous cutoff wave length of Donelan and Pierson. In other words, the modeled Donelan and Pierson short wave spectrum was found to be too sensitive to the effects of water viscosity. Clear experimental evidence of this was also given by *Jähne and Riemer* [1990], who, in the framework of the VIERS project, measured the slope spectrum by means of optical techniques. Even for low wind speed, considerable contributions to the slope spectrum were found at wave number k = 800 rad/m, which is well beyond the viscous cutoff of Donelan and Pierson. *Apel* [1994] has summarized the findings of *Jähne and Riemer* [1990] and *Klinke and Jähne* [1992] in terms of a semiempirical model for the short wave spectrum.

Also, shortcomings in the electromagnetics part of the *Donelan and Pierson* [1987] scatterometer algorithm were found. In order to shield off a singularity in the Bragg scattering near nadir, a cutoff condition was applied when the local incidence angle was <18°. Nevertheless, for small incidence angle the contribution of Bragg scattering dominates the one of specular reflection, which is unexpected. Furthermore, the choice of the cutoff wave number is not always adequate. For example, for the wave tank data the dominant wave has a much larger wave number than at sea, sometimes even beyond k_c.

In order to alleviate the above mentioned problems it was decided to develop a new scatterometer algorithm. In particular, regarding the electromagnetic part, the introduction of a cutoff wave number on a more or less physical basis was considered. Furthermore, it was decided to remove the cutoff condition near nadir and to add the specular reflection. Finally, it was thought to include more physics in the energy balance equation, because nonlinear wave-wave interactions and effects of slicks may be relevant processes as well in determining the short wave spectrum.

Before our attempt to improve on the *Donelan and Pierson* [1987] scatterometer model is described, it is emphasized that a basic assumption of the VIERS scatterometer model is that wind wave generation is determined by the surface stress. At the air-sea interface the stress field is determined by the wind speed, the stability of the air column, and the sea state, which we characterize by the wave age of the wind sea. In order to obtain the stress τ or the friction velocity u_* the wind profile $U(z)$ is assumed to have the form

$$U(z) = \frac{u_*}{k}[\log (z/z_0) - \psi(z/L)] \tag{2}$$

Here the roughness length includes the effects of the sea state and is parameterized according to *Smith et al.* [1992]

$$z_0 = \alpha \frac{u_*^2}{g} \qquad \alpha = 0.48(c_p/u_*)^{-1} \tag{3}$$

where c_p/u_* is the age of the wind sea and c_p is the phase speed of the peak of the wind sea spectrum.

For the stability function ψ we adopt the Businger-Dyer expression [*Businger et al.*, 1971; *Dyer and Hicks*, 1970]. For stable conditions ($L > 0$) we have

$$\psi = -z/L$$

while for unstable conditions ($L < 0$) we take

$$\psi = \frac{\pi}{2} + 2 \log [(1 + \Phi)/2] + \log [(1 + \Phi^2)/2] - 2 \tan \phi \tag{4}$$

where

$$\Phi = (1 - 16z/L)^{0.25} \tag{5}$$

and the Monin-Obukov length is computed according to *Stewart* [1985]

$$L = \frac{-u_* U(z)}{g\kappa} \frac{T_{\mathrm{air}}}{T_{\mathrm{sea}} - T_{\mathrm{air}}} \tag{6}$$

with g as the acceleration of gravity, κ as the von karman constant, T_{air} as the air temperature, and T_{sea} as the water temperature.

For given wind speed, phase speed of the waves, air temperature, and sea temperature the friction velocity u_* is solved from (2) in an iterative manner.

2.1. Short Wave Model

The model for the short wave spectrum is based on the energy balance equation, which is solved under steady state circumstances because the short waves have a very short response timescale. Also, advection of short wave energy is disregarded, and the energy balance equation therefore reads

$$S_{\mathrm{in}} + S_{\mathrm{nonl}} + S_{\mathrm{visc}} + S_{\mathrm{br}} + S_{\mathrm{slicks}} = 0 \tag{7}$$

where S_{in} represents the effects of wind stress, S_{nonl} describes three- and four-wave interactions, S_{visc} describes viscous dissipation, S_{br} describes dissipation due to whitecapping, and S_{slicks} describes the resonant energy transfer between surface waves and slicks (Marengoni effect). The energy balance equation (7) is solved as a boundary value problem in wave number space by providing the energy flux from the long to the short waves at a boundary $k = k_{join} \simeq g/u_*^2$, which corresponds to $c/u_* \simeq 1$ with c as the phase speed of gravity waves.

In order to determine the energy flux at the boundary $k = k_{join}$, knowledge of the gravity part of the wave spectrum is required. In general, the long wave spectrum consists of wind sea and swell, and the simplifying assumption is made that the energy flux at k_{join} is mainly determined by the wind sea part of the spectrum since swell usually has a small steepness. The one-dimensional wind sea wave number spectrum is assumed to be given by the Joint North Sea Wave Project (JONSWAP) shape [*Hasselmann et al.*, 1973], which is obtained from the frequency spectrum by using the linear dispersion relation for gravity waves. Hence

$$F(k) = \tfrac{1}{2}\alpha_p k^{-4} \exp\left[-\frac{5}{4}\left(\frac{k_p}{k}\right)^2\right]\gamma^r \tag{8}$$

where

$$r = \exp\left[\frac{-(k^{1/2} - k_p^{1/2})^2}{2\sigma^2 k_p}\right]$$

In JONSWAP, steady state conditions were considered, and therefore the spectral parameters k_p, α_p, γ, and σ were only determined as a function of dimensionless fetch. The sea state will depend on both duration and fetch, however. In order to accommodate both circumstances, the spectral shape parameters are assumed to depend on the wave age

$$\chi = c_p/u_* \tag{9}$$

where u_* is the friction velocity and c_p is the phase speed of the peak of the wind sea spectrum, which in principle may be obtained from an ocean wave prediction model (e.g., the WAM model) [cf. *Komen et al.*, 1994]. Thus

$$\begin{gathered} k_p = g/c_p^2 \\ \alpha_p = A\chi^{-B} \\ \gamma = \max\left[1,\ 1 + 3(1 - (0.038\chi)^2)\right] \\ \sigma = 0.08 \end{gathered} \tag{10}$$

The parametrization of the Phillips parameter α_p was not obtained from JONSWAP, because in the JONSWAP fit for α_p, laboratory data were also used which, as is known from *Donelan et al.* [1985], belong to a different family. In a tuning exercise with the full VIERS model it was found that

$$A = 0.24$$

$$B = 1$$

gave satisfactory results. This choice of parameters for the Phillips parameter is in fair agreement with the reanalysis of JONSWAP data performed by *Günther* [1981]. Furthermore, JONSWAP only considered young wind sea cases with a peak enhancement factor γ, which was on average 3.3. In order to assure that for old wind sea the JONSWAP spectrum asymptotes to the Pierson Moskowitz spectrum (hence $\gamma \to 1$), we have added the χ^2 factor in the expression for γ.

The JONSWAP spectrum is strictly speaking only valid for wave numbers up to 9 times the peak wave number. Recent observations of *Banner* [1990] confirm that up to a wave number of 30 rad/m the wave spectrum indeed follows a k^{-4} law, thus the region of validity of the JONSWAP spectrum may be extended to these high wave numbers. The present parameterization of the high wave number tail of the gravity wave spectrum differs, however, in one important aspect from Banner's fit to his observations. He chose a less sensitive dependence of the Phillips parameter on wave age (namely in his case B = 0.5), but the data contained only one young wind sea case. On the other hand, our parameterization is not in conflict with the data of *Jähne and Riemer* [1990], who found in the Delft wave tank a linear dependence of the gravity wave part of the spectrum on friction velocity which agrees with (10) with $B = 1$.

For wave numbers higher than k_{join} a new regime is entered because three wave interactions start to play a role in the steady state energy balance of the short waves (equation (7)). In the following we shall only develop a theory for the one-dimensional wave number spectrum, while the angular distribution of the short waves is modeled in a fairly simple fashion. The main reason for this is that we were unable to derive a reasonable parameterization of the angular dependence of the nonlinear interactions.

The one-dimensional wave number spectrum $F(k)$, which is related to the Fourier transform of the autocorrelation of the surface elevation, is normalized in such a way that $\int_0^\infty F(k)k\,dk = E$, where E is the wave variance. The wave energy density $\mathscr{E}$ follows then from

$$\mathscr{E}(k) = \frac{\omega^2}{k} F(k) \tag{11}$$

where we shall only consider pure gravity-capillary waves with dispersion relation

$$\omega(k) = \sqrt{gk + Tk^3} \tag{12}$$

with g as acceleration of gravity and T as surface tension. Hence effects of current and shear in the current will be neglected.

Let us now describe some of the details of the source terms in the energy balance (7). For the input source term we adopt *Plant*'s [1980] expression

$$S_{in} = \beta F \qquad \beta = \delta\omega\left(\frac{u_*}{c}\right)^2 \tag{13}$$

where the dimensionless constant δ is given the value 0.03. The slowing down of wind by the short waves (the so-called quasi-linear effect) can be incorporated by renormalizing δ [cf. *Janssen et al.*, 1989; *Snoeij et al.*, 1993]. As a result, the wind input to the steep waves is reduced which has in practice a considerable impact on the backscatter which may be reduced by 5 dB.

Although *Donelan and Pierson* [1987] did not take effects of nonlinear three- and four-wave interactions into account, the work of *Valenzuela* [1978], *van Gastel* [1987], and *Janssen* [1987] suggests that three-wave interactions play an important role in the dynamical evolution of gravity-capillary waves, while *Kitaigorodskii* [1983] and *Phillips* [1985] stress the importance of four-wave interactions for short gravity waves. The exact expressions for three- and four-wave interactions obtained by *Davidson* [1972], *Valenzuela* [1978], and *Hasselmann* [1962] will be used as a guideline to obtain an efficient parameterization of the nonlinear transfer.

Following *Kitaigorodskii* [1983], we assume that the nonlinear transfer is a local process in wave number space, and introducing the energy flux $\varepsilon(k)$, one thus has

$$S_{\mathrm{nl}} = -\frac{1}{k}\frac{\partial}{\partial k}\,\varepsilon(k) \tag{14}$$

and on dimensional grounds the expression for ε reads

$$\varepsilon(k) = \frac{c^4}{v_g}\,[\alpha_3 B^2 + \alpha_4 B^3] \tag{15}$$

where v_g is the group velocity $\partial\omega/\partial k$, B is the angular average of the degree of saturation [*Phillips*, 1985],

$$B = k^4 F(k) \tag{16}$$

while α_3 and α_4 give the strength of the three- and four-wave interactions, respectively. The coefficients α_3 and α_4 may still depend on the ratio c/v_g. In particular, α_3 should vanish in the gravity wave regime because three-wave interactions are not possible there.

Three dissipative processes are assumed to play a role in the gravity-capillary regime, namely, viscous dissipation, wave breaking, and damping due to slicks. For viscous damping we use the exact expression [*Lamb*, 1932],

$$S_{\mathrm{visc}} = -4\nu k^2 F \tag{17}$$

where ν is the kinematic viscosity of water.

Damping by slicks is caused by the Marangoni effect [*Alpers and Hühnerfuss*, 1989], which is the result of a resonant interaction between a sound wave in the surface film and short gravity waves. The Marangoni effect gives rise to an enhanced viscous damping

$$S_{\mathrm{slicks}} + S_{\mathrm{visc}} = -4\nu_{\mathrm{eff}} k^2 F \tag{18}$$

where

$$\nu_{\mathrm{eff}} = \nu M(k, \nu, \delta, E_s) \tag{19}$$

with M a relative damping ratio given by

$$M = \frac{1 + X(\cos\delta - \sin\delta) + XY + Y\sin\delta}{1 + 2X(\cos\delta - \sin\delta) + 2X^2} \tag{20}$$

δ is a phase angle and

$$X = \left|\frac{E_s}{\rho_w}\right|\frac{k^2}{\sqrt{2\nu\omega^3}} \qquad Y = \left|\frac{E_s}{\rho_w}\right|\frac{k}{4\omega\nu} \tag{21}$$

Furthermore, E_s is the dilational modulus of the surface film, and ρ_w is the density of water. The surface film is determined by the two parameters δ and E_s. The phase angle δ is ~180°, whereas E_s depends strongly on the type of slick. For a natural slick, mostly of biological origin, E_s may have the value of 0.01 N/m, whereas for chemical slicks its value may vary between 0.01 and 0.05 N/m.

Slicks may be destroyed, however, by the action of wind. We have modeled this by letting the dilational modulus vanish for strong enough winds, $E_s = 0.005[1 - \tanh(10u_* - 4.33)]$. In addition, since it is unrealistic that the ocean is covered by a single large slick, a second modification was implemented. Since slicks come in patches, there is need for a fractional filling factor F [*Lombardini*, 1986]. With $F \le 1$ the damping is modified according to $M_F = M/[M + F(1 - M)]$, where M is the damping when the coverage is complete. Typical F values are in the range 0.88–0.99.

It is remarked that in case of open ocean wind retrieval we have chosen to include an average effect of slicks for low wind speed. However, when comparing results from our spectral model with our laboratory data, the effect of slicks is switched off, because the experimentalists made sure that the water surface was clean so that no slicks were present. This was achieved by having an overflow at the end of the wind wave tank and by running the tank for a sufficiently long time so that after visual inspection, films had disappeared.

Individual breaking events are difficult to model because of strong nonlinearity. In a statistical description of wave evolution the whitecaps cover only a relatively small fraction of the surface, and whitecapping may therefore be regarded as a process which is weak in the mean. In work by *Komen et al.* [1994] it is then shown that the corresponding source term is quasi-linear; it consists of the spectrum at the wave number considered multiplied by a factor which is a function of the entire spectrum. Extending the *Komen et al.* [1984] expression for gravity wave dissipation into the gravity-capillary regime, we take

$$S_{\mathrm{br}} = -\beta_d\bar{\omega}(\bar{k}^2E)^2(k/\bar{k})F(k) \tag{22}$$

where β_d is a constant of the order 2, and $\bar{\omega}$ and $\bar{k}$ are mean angular frequency and wave number, while E is the wave variance.

Combining now the explicit expressions for the source terms, the energy balance equation (7) becomes

$$\frac{\partial}{\partial k}\,\varepsilon(k) = \gamma\,\frac{\omega^2}{k^4}\,B \tag{23}$$

where the parameter γ is defined as

$$\gamma = \delta\omega\left(\frac{u_*}{c}\right)^2 - 4\nu M k^2 - \beta_d\bar{\omega}(\bar{k}^2E)^2(k/\bar{k}) \tag{24}$$

and hence gives the net effect of wind input and dissipation. The energy flux $\varepsilon(k)$ is given by

$$\varepsilon(k) = \frac{c^4}{v_g}\,(\alpha_3 B^2 + \alpha_4 B^3) \tag{25}$$

and we have eliminated the wave number spectrum F in favor of the degree of saturation $B = k^4F$.

The interaction coefficient α_4 for four-wave interactions is taken as a constant, $\alpha_4 \simeq 0.25$, while α_3 is allowed to depend on wave number because it is assumed that for gravity waves, three-wave interactions are not important. We take

$$\alpha_3 = \frac{3\pi}{16}\,\{\tanh[\sigma_3(x - 1)] + 1\}$$

where $x = (k/k_{\mathrm{join}})^{1/2}$ and $\sigma_3 = 2$. We remark that this choice of α_3 is, to a certain extent, arbitrary; however, a continuous transition from vanishing α_3 in the gravity range to a constant value in the gravity-capillary range is needed to avoid jumps in the spectrum.

By supplying the boundary condition at $k = k_{\mathrm{join}}$ of continuity of flux (or spectrum) the differential equation (23) may be solved for the degree of saturation B, and the wave number

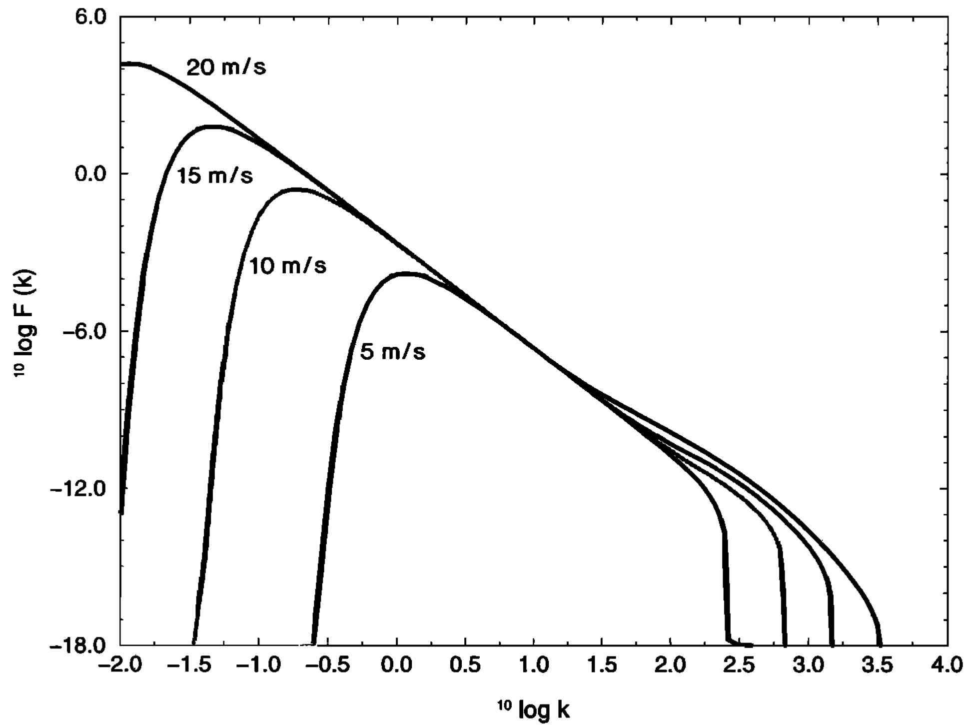

Figure 2. Wave number spectrum versus wave number for wind speeds of 5, 0, 15, and 20 m/s. The wave age parameter is 25.

spectrum $F(k)$ follows. In combination with the JONSWAP spectrum for $k < k_{\mathrm{join}}$ the full one-dimensional wave number spectrum is obtained. Examples of the one-dimensional wave number spectrum according to the VIERS model equation (23) are shown in Figure 2 for four different friction velocities and old wind sea (wave age $\chi \simeq 25$). The sensitive dependence of the high wave number part of the spectrum on friction velocity should be emphasized; this is, of course, the main reason why a scatterometer, which "observes" waves with wave numbers larger than 100, may be used as an instrument for measuring the wind field above the oceans.

In order to perform a successful wind retrieval the two-dimensional wave number spectrum is required. To that end we have taken a simple directional distribution $D(\phi)$

$$D(\phi) = \frac{1}{2\pi}[1 + 2a_2 \cos 2(\phi - \phi_w)] \qquad (26)$$

where ϕ is the wave direction, ϕ_w is the wind direction, and a_2 is a parameter which measures the width of the directional distribution; a_2 is assumed to depend on friction velocity only and not on wave number. The two-dimensional wave number spectrum is then given by

$$W(k, \phi) = F(k)D(\phi) \qquad (27)$$

and it will be used in a two-scale model to obtain the normalized backscatter.

We would like to discuss briefly some of the properties of the energy balance equation (23). In addition, modeled spectra are compared with observed spectra obtained in the Delft wave tank.

Since in practice the degree of saturation B is of the order 0.1 or less, it is a fair approximation to disregard four-wave interactions in the expression for the energy flux, (25). Retaining therefore only three-wave interactions, the energy balance equation (23) may be solved, and the result for the degree of saturation becomes

$$B = \left(\frac{v_g}{\alpha_3}\right)^{1/2} c^{-2}\left\{\varepsilon_0^{1/2} + \frac{1}{2\alpha_3^{1/2}}\int_{k_{\mathrm{join}}}^{k} dk\, \frac{\gamma}{k^2}\sqrt{v_g}\right\} \qquad (28)$$

where ε_0 is the value of the energy flux at $k = k_{\mathrm{join}}$. It is of interest to discuss the respective terms in (28) separately. The first term is related to the effect of three-wave interactions. In the absence of wind input and dissipation it follows from the condition of a constant energy flux in wave number space. Using the dispersion relation for pure gravity-capillary waves (equation (12)), the degree of saturation according to the constant energy flux condition becomes

$$B_{3w} = \left(\frac{\varepsilon_0}{2\alpha_3}\right)^{1/2} c_0^{-3/2} \frac{y(1+3y^2)^{1/2}}{(1+y^2)(y+y^3)^{1/4}} \qquad (29)$$

where $y = k/k_0$, $k_0 = (g/T)^{1/2}$ is the wave number that separates gravity waves and capillary waves, and $c_0 = (gT)^{1/4}$. Therefore, in the gravity wave range ($k < k_0$), the degree of saturation increases with wave number like $k^{3/4}$ while, in the capillary wave range, B_{3w} decreases with wave number like $k^{-3/4}$ and B_{3w} attains its maximum value around $k = k_0$.

Effects of wind input and dissipation (γ) are represented by the second term in (28) and result in a modification of the "inertial" subrange spectrum given in (29). The degree of saturation now becomes a sensitive function of the friction velocity while, for large wave numbers, dissipation becomes important. For a large enough wave number the degree of saturation B will vanish. Let us call this particular wave number the cutoff wave number. In order to be able to compare with results from

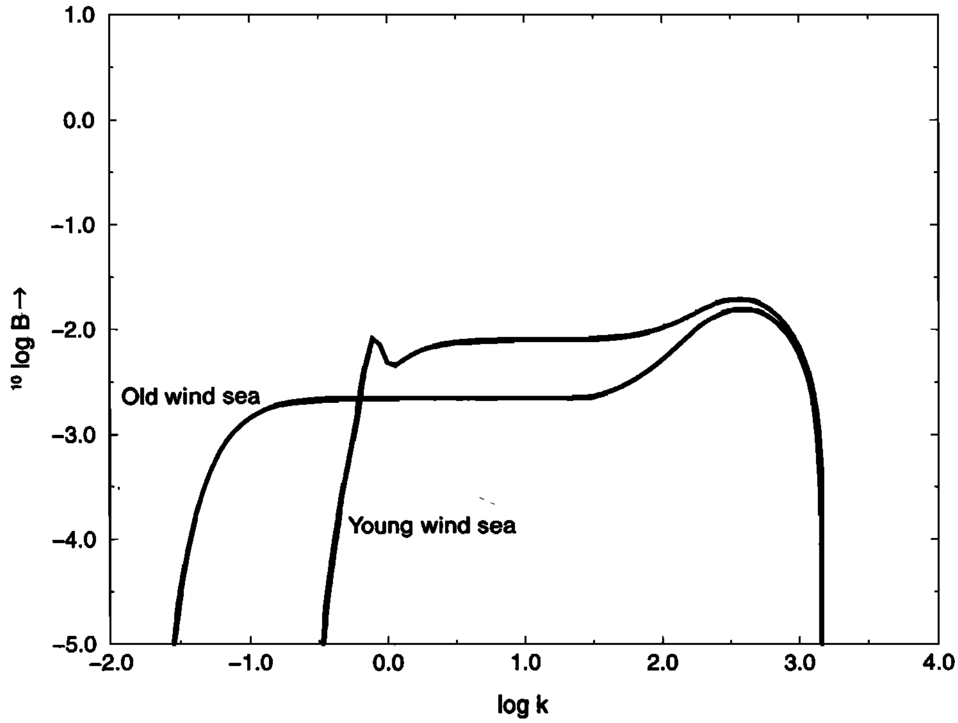

Figure 3. Comparison of degree of saturation $B(k)$ as function of wave number for young and old wind sea. The wind speed is 15 m/s.

the *Donelan and Pierson* [1987] model, we shall retain, in γ of (24), only the effects of wind input and viscous dissipation. Hence the cutoff wave number is determined by viscosity, and the viscous cutoff wave number in the Donelan and Pierson model follows from the condition $\gamma = 0$, or

$$\omega = \frac{1}{4}\frac{\delta u_*^2}{\nu} \tag{30}$$

In the present model, B does not depend on the local value of γ but depends on an integral in wave number space involving γ. As a consequence, the viscous cutoff wave number shifts to much larger values than given by (30). This shift in cutoff wave number is caused by the nonlinear energy transfer, which tries to maintain an inertial subrange spectrum. As a result, the present model therefore has a reduced sensitivity to changes in the water viscosity, at least in the wave number range that is relevant for scatterometry.

Furthermore, it is noted that ε_0, which is determined by the JONSWAP spectrum (8), contains all the effects of sea state (i.e., wave age of long waves) on the short wave spectrum. As an illustration, we have compared in Figure 3 the degree of saturation B for young wind sea ($\chi \simeq 7$) with old wind sea ($\chi \simeq 25$), and the sea state dependence may be quite considerable, in particular in the low wave number range. From Figure 3 it is also noted that for young wind sea the increase of B in the high wave number range is less pronounced than in the case of old wind sea, which suggests that for young wind sea the short wave spectrum is controlled by nonlinear transfer because the short gravity waves are steeper.

We conclude this subsection by comparing results of the present short wave model with observed frequency spectra in the Delft wave tank. Frequency spectra were measured by means of a Lobemeier wire and a laser slope gauge (LSG) of *Jähne and Riemer* [1990] for different friction velocities and fetches. Lobemeier spectra are thought to be reliable up to a frequency of 10 Hz, while LSG spectra are supposed to be valid to at least 100 Hz. If the Doppler shift due to the orbital motion of the long waves is ignored (this is a reasonable assumption in a wave tank), the modeled frequency spectrum $E(f)$ may be obtained from the wave number spectrum $F(k)$ according to

$$E(f) = \frac{2\pi k}{v_g} F(k)$$

where the group velocity v_g is obtained for the dispersion relation of pure gravity-capillary waves (equation (12)). Examples of the comparison between observed and modeled frequency spectra are shown in Figure 4 for two different friction velocities and a fetch of 90 m. In view of the differences that do exist between the two types of observed spectra it may be concluded that the present short wave model shows a fair agreement with the observations. Furthermore, for comparison purposes we have plotted for the high friction velocity case the *Donelan and Pierson* [1987] short wave spectrum, and considerable differences with the observed wave tank spectra are found. The reason for this is that the Donelan and Pierson spectrum has an f^{-5} shape while the observed spectra in this frequency range have an f^{-4} shape. Finally, it is remarked that the water surface in the wave tank was clean, hence effects of slicks were disregarded. For low wind speed, slicks may have a dramatic impact on the spectral shape as is illustrated in the low wind speed case of Figure 4.

2.2. Radar Backscatter Model

Once the two-dimensional wave spectrum is known, the normalized backscatter may be obtained by means of a two-scale

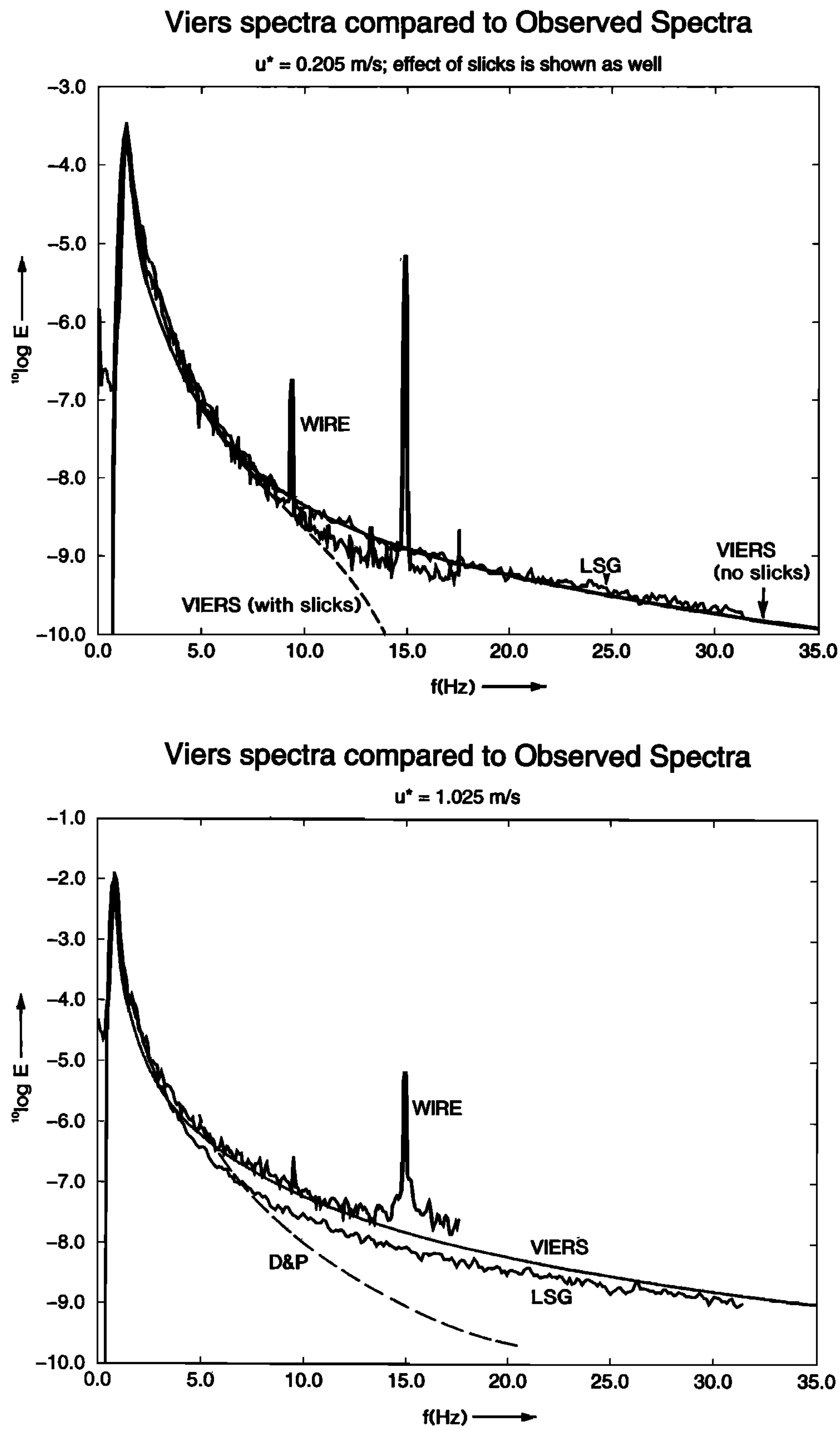

Figure 4. Comparison of simulated and laboratory frequency spectra for a friction velocity of 0.205 and 1.025 m/s, respectively, and a fetch of 90 m. For the low friction velocity case the impact of slicks on spectral shape is shown as well, while for the high friction velocity case we show the short wave spectrum according to *Donelan and Pierson* [1987] (D&P).

model. According to the wave-facet model [*Plant*, 1990] the normalized cross section is given by

$$\sigma_0 = \sigma_0^{\mathrm{sp}} + \int_{-\infty}^{\infty} d(\tan\psi)\int_{-\infty}^{\infty} d(\tan\delta)P_B(\tan\psi,\ \tan\delta)\sigma_0^{\mathrm{Br}}(\theta_l) \tag{31}$$

where P_B is the probability that a (Bragg) facet is oriented with tilts $\tan\psi$ and $\tan\delta$ along-wind and crosswind, respectively, while θ_l is the local incidence angle. For an anisotropic Gaussian surface one has

$$P_B = \frac{1}{2\pi s_{u,b}s_{c,b}}\exp\left(-\frac{\tan^2\psi}{2s_{u,b}^2} - \frac{\tan^2\delta}{2s_{c,b}^2}\right) \tag{32}$$

with $s_{u,b}^2$ and $s_{c,b}^2$ as the slope variances in upwind and crosswind. The Bragg contribution of a facet is proportional to the two-dimensional wave number spectrum at the Bragg wave number k_b (compare (1)). In fact,

$$\sigma_0^{\mathrm{Br}} = 8\pi k_R^4 \cos^4\theta_l |g_{\mathrm{pol}}|^2[W(\mathbf{k}_b) + W(-\mathbf{k}_b)] \tag{33}$$

with k_R as the radar wave number and g as a factor which depends on the polarization. The contribution due to specular reflection is given by

$$\sigma_0^{\mathrm{sp}} = \pi|R(0)|^2 \sec^4\theta P(\zeta_x,\ \zeta_y) \tag{34}$$

where P is the probability that a specular facet is oriented with tilts ζ_x and ζ_y parallel and at right angles to the radar look direction, respectively. For an anisotropic Gaussian surface one has

$$P = P(\zeta_x = \tan\theta,\ \zeta_y = 0) = \frac{1}{2\pi s_{u,s}s_{c,s}}\exp\left(-\frac{\tan^2\theta}{2s_{L,s}^2}\right) \tag{35}$$

with $s_{u,s}^2$ and $s_{c,s}^2$ as the slope variances in the upwind and crosswind direction, whereas $s_{L,s}^2$ is the variance in the radar look direction. Only those waves that have a wavelength longer than the radar wavelength contribute to the slope variances as shorter waves are not seen by the radar [*Stewart*, 1985]. Furthermore, $|R(0)|^2$ is the reflection coefficient at normal incidence, which depends on the radar frequency via the relative dielectric constant ε_r

$$|R(0)| = |0.65(\varepsilon_r - 1)/(\sqrt{\varepsilon_r} + 1)^2|.$$

The factor 0.65 in this last equation is based on a correction of the standard reflection coefficient as specified by *Valenzuela* [1978]. The correction factor is needed because the remaining short wave disturbances of the water surface reduce the cross section as given by physical optics.

The above general two-scale theory has to be supplemented with a criterion to separate long waves from short ones. The wave number spectrum is separated into a low and high wave number part by means of the separation scale k_c

$$W_L(k,\ \phi) = \begin{cases} W(k,\ \phi) & k < k_c \\ 0 & k > k_c \end{cases}$$
$$W_H(k,\ \phi) = \begin{cases} 0 & k < k_c \\ W(k,\ \phi) & k > k_c \end{cases} \tag{36}$$

Hence, using the directional distribution (26), the slope variances of the tilting waves are given by

$$s_{u,b}^2 = \frac{1 + a_2}{2}\int_0^{k_c} k^3F(k)\ dk \tag{37}$$

$$s_{c,b}^2 = \frac{1 - a_2}{2}\int_0^{k_c} k^3F(k)\ dk$$

while the slope variance of the waves that contribute to specular reflection is given by $s_{L,s}^2 = s_{u,b}^2 + s_{c,b}^2$. Finally, the separation scale k_c is determined by the condition

$$\beta = 4k_R^2\sigma_H^2 \qquad \sigma_H^2 = \int_{k_c}^{\infty} F(k)\ dk \tag{38}$$

Condition (38) follows from the work of *Bahar et al.* [1983] and *Brown* [1978]. An optimal choice for the parameter β is then found to lie in the range 0.1–1. On the basis of a comparison with the VIERS data set [*Snoeij et al.*, 1993], $\beta = 0.13$ turns out to give optimal results for the normalized backscatter.

The present version of the two-scale model was tested against observed data obtained during the VIERS tank experiment at Delft Hydraulics. The radar operated at X band. Observed wave spectra were used as input to the backscatter algorithm. Figure 5 shows the normalized radar cross section σ (in decibels) as a function of incidence angle for vertical and horizontal polarization. The fetch was 90 m, and the friction velocity was $u_* = 0.367$ m/s. From Figure 5 it is concluded that there is a fair agreement between modeled and observed backscatter for vertical polarization but that the modeled backscatter is too low by as much as 5 dB for horizontal polarization. A similar poor performance at horizontal polarization was noted with *Plant*'s [1990] composite surface model.

Finally, we show for C band the dependence of modeled backscatter on incidence angle for several wind speeds, where we used the parameterizations for the wind sea spectrum as appropriate for oceanic conditions. The sea state was assumed to be fully developed; for young wind seas the backscatter would increase by about 3 dB for incidence angles larger than 25°.

3. Inverse VIERS Model

The VIERS model consists of the three principal components discussed in section 2, namely, (1) a module to determine the stress for given wind, air-sea temperature difference and sea state; (2) a module to determine the short wave spectrum for given stress and sea state of the long wind waves; and (3) a module to obtain the normalized backscatter for a given two-dimensional wave spectrum. Therefore the VIERS model relates radar backscatter to wind vector, measurement geometry (e.g., incidence angle), sea state, air-sea temperature difference, and slicks. In most applications an averaged effect of slicks will be taken into account while effects of atmospheric stability on the stress will be disregarded. However, when studying some synoptic cases near the Norwegian coast, stratification may be important, and in section 4.2 it is shown that inclusion of stratification has a favorable impact on wind retrieval.

For the practical application of wind retrieval from (ERS-1) scatterometer data the model has to be inverted, however. In order to achieve this the following simple, straightforward procedure was adopted.

A table of normalized backscatter σ_0 is produced; the VIERS model is run for different incidence angles, wind vectors, and wave periods (or peak phase speeds) and the resulting σ_0 values are collected in a table. The wind parameters are wind

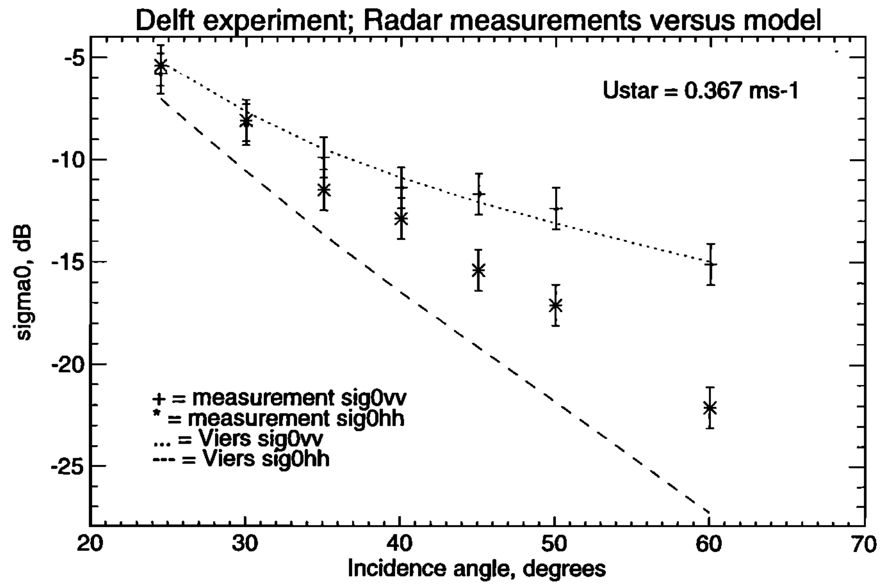

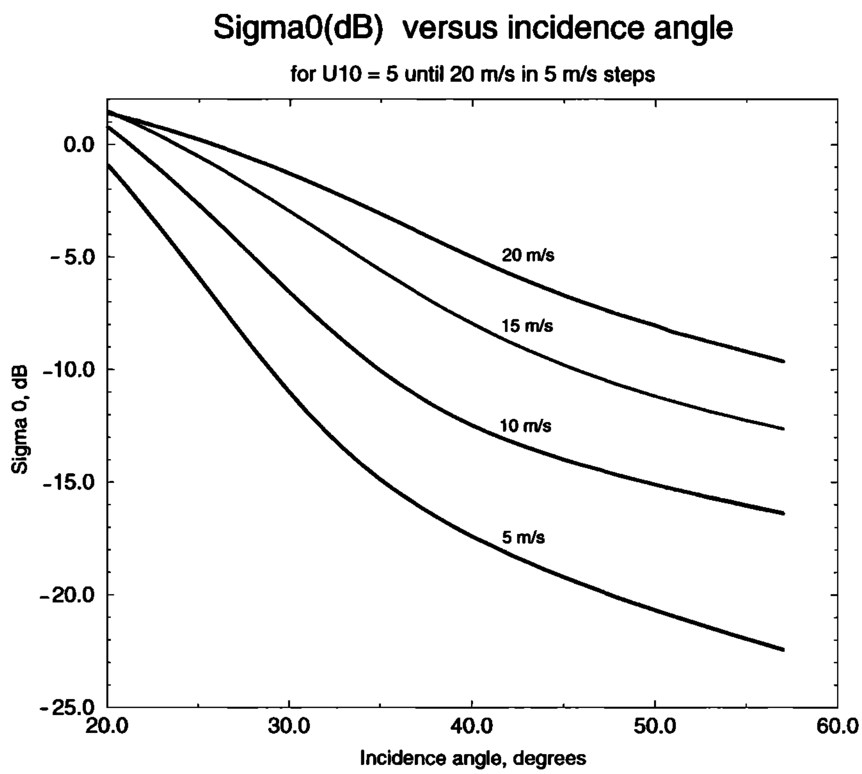

Figure 5. (top) Comparison of simulated and observed backscatter from the Delft wave tank as a function of incidence angle for a friction of 0.367 m/s, a fetch of 90 m, and two different polarizations. (bottom) Simulated backscatter as a function of incidence angle for different wind speeds for oceanic conditions.

speed U and the direction ϕ with respect to the look direction of the radar. If one accepts an accuracy of 1 m/s in retrieved wind speed and 15° in the wind direction, the incidence angle may be chosen in the range of 18° until 57° in steps of 1°, U from 1 until 30 m/s in steps of 1 m/s, and ϕ in steps of 15°, for instance.

The inversion procedure we adopted is specific for the ERS-1 configuration, where, for a certain cell i, three measurements of radar backscatter for different look angle and incidence angle were performed. The measured sigma triplet is denoted by $(\sigma_f, \sigma_m, \sigma_a)$, where the subscripts denote fore, middle, and aft beam, respectively. The wind retrieval procedure is then as follows.

1. Determine incidence angles of fore, middle, and aft beam: $\theta_f(i)$, $\theta_m(i)$, $\theta_a(i)$.

2. Calculate the corresponding model triplets for all tabulated wind vectors according to

$$\begin{aligned}\sigma_f^{\mathrm{mod}} &= \sigma^{\mathrm{tab}}(\theta_f, U, \phi + 45, c_p)\\ \sigma_m^{\mathrm{mod}} &= \sigma^{\mathrm{tab}}(\theta_m, U, \phi, c_p)\\ \sigma_R^{\mathrm{mod}} &= \sigma^{\mathrm{tab}}(\theta_a, U, \phi - 45, c_p)\end{aligned} \tag{39}$$

Here ϕ is the wind direction with respect to the midbeam, and c_p is the wind sea phase speed obtained from a wave prediction model (e.g., the WAM model [*Komen et al.*, 1994]).

3. Determine the normalized quadratic distance between modeled and measured triplets,

$$Q_{\text{ERS-1}} = \sum_{n=1}^{n_b} Q_n \tag{40}$$

where the index n refers to the beam ($n_b = 3$) and

$$Q_n = \left(\frac{\sigma_n - \sigma_n^{\text{mod}}}{k_p \sigma_n} \right)^2 \tag{41}$$

Here k_p is the relative accuracy of the measurement (of the order of 5%), and $k_p \sigma_n$ is the measurement error in σ.

4. Determine the normalized quadratic distance between retrieved and ECMWF wind (both magnitude and direction)

$$Q_{\text{GEO}} = \left(\frac{U - U_{\text{GEO}}}{\Delta U_{\text{GEO}}} \right)^2 + \left(\frac{\phi + \chi_m - \phi_{\text{GEO}}}{\Delta \phi_{\text{GEO}}} \right)^2 \tag{42}$$

where χ_m is the look direction of the midbeam with respect to north. The errors in the ECMWF wind fields are estimated to be $\Delta U_{\text{GEO}} = 2$ m/s and $\Delta \phi_{\text{GEO}} = 20°$.

5. Determine for all 30 × 24 tabulated wind vectors the cost function D

$$D = \sqrt{Q_{\text{ERS-1}} + Q_{\text{GEO}}} \tag{43}$$

and infer its absolute minimum.

6. The model wind that minimizes D is called the retrieved wind. The wind direction with respect to true north, ϕ_w, is given by $\phi_w = \chi_m + \phi_{\text{ret}}$, where ϕ_{ret} is the retrieved wind direction with respect to the midbeam.

The fourth step is inserted in order to remove the ambiguity in direction of 180°. This is a well-known problem in scatterometry and is evident from expression (33) of the Bragg contribution to the radar backscatter. Thus the ambiguity problem is removed by step 4, but one may introduce a spurious interdependence between retrieved and ECMWF winds.

The choice of using tabulated values of backscatter to evaluate the cost function has certain advantages. The modern approach to inversion would be to minimize the cost function using the adjoint of the forward model. However, we thought that it was far too much effort to write the adjoint of the model, while from experience it was known that the forward VIERS-1 model was too expensive to run in an operational context. The introduction of a table is far less expensive. In addition, the search for a minimum of the cost function is straightforward as the cost function may be evaluated for all possible wind speeds and directions. The added advantage is that there is no need to write an adjoint of the VIERS-1 model.

Before we discuss, in the next section, results for wind retrieval with the VIERS algorithm, it is of importance to briefly comment on the tuning procedure we followed. Several parameters in the short wave model are not fixed a priori, the most important ones being k_{join}, the directional width parameter a_2, and the Phillips parameter α_p. However, it should be emphasized that there are empirical guidelines for the choices of a_2 and α_p. Nevertheless, the model output depends critically on the precise choice of k_{join}, a_2 as a function of u_*, and α_p as a function of wave age. These three variables were the basic tuning parameters.

Initially, we tuned the "forward" VIERS algorithm. Thus the simulated backscatter, obtained using ECMWF winds and WAM model periods, was compared with the backscatter as observed by ERS-1. After some tuning a reasonable agreement between simulated and observed backscatter was obtained. We typically found a standard deviation of error of about 2 dB in σ_0, which in view of the limited knowledge of the spectrum of short waves and in view of the accuracy of the analyzed wind field (which we assume to be 2 m/s) is already quite an achievement. We were therefore quite optimistic that the thus obtained algorithm would be successful in retrieving winds from the observed radar backscatter. Unfortunately, this turned out not to be the case, and some additional tuning was required to obtain reliable winds. The main reason for the additional tuning is that we needed an accuracy of the model algorithm of at least 0.5 dB, which cannot be achieved using analyzed winds with a relatively large error in magnitude (±2 m/s) and direction (±15°). The quality of the analyzed winds obtained from the ECMWF analysis and forecasting system has been studied extensively by comparing modeled and observed wind speed form buoys over a 1-year period [*Janssen et al.*, 1997]. As a result, it is found that the ECMWF winds have on average a rms error of about 2 m/s, and this estimate of the wind speed error has been used in the cost function (42).

It was therefore decided to use the inverse of the VIERS model to do the tuning. To that end, about 30,000 σ_0 triplets, measured with the ERS-1 scatterometer (operating at C band) on November 6, 1991, together with collocated periods from the WAM model, were supplied to the inverted VIERS model. The resulting retrieved winds (magnitude and direction) were plotted against collocated analyzed winds obtained from the ECMWF atmospheric model. The tuning parameters k_{join}, a_2, and α_p were chosen in such a way that the average bias and scatter index (between VIERS and ECMWF winds) were as low as possible and the spectra from the short wave model were of the best quality. This approach ensures that the VIERS and ECMWF winds are compatible in a statistical sense, while also reasonable choices for the tuning parameters have been obtained. For example, the wave age dependence of the Phillips parameter, as given in (10), is in fair agreement with *Günther*'s [1981] reanalysis of the JONSWAP data.

The tuned VIERS algorithm has been used to produce the plots depicted in Figures 6 and 7. In order to visualize the density of points, contour lines of equal density (number of points per square m/s cq°) are drawn. As a reference, we have produced the same plots with the CMOD4 model, using the same inversion technique. It can be seen that the VIERS is well tuned in the sense that it produces winds that are compatible with the analyzed ECMWF winds.

4. Wind Retrieval With the VIERS Algorithm

In this section we would like to present our results for wind retrieval with the VIERS algorithm. Results are compared in detail with analyzed wind fields from ECMWF and with retrieved winds from the CMOD4 algorithm. Two approaches are followed. In section 4.1 we shall use statistical tools to compare results. while in section 4.2 we give a comparison of results with emphasis on synoptic situations. It is felt that these two approaches are to some extent complementary, and they will highlight the strong and weak points of the VIERS algorithm.

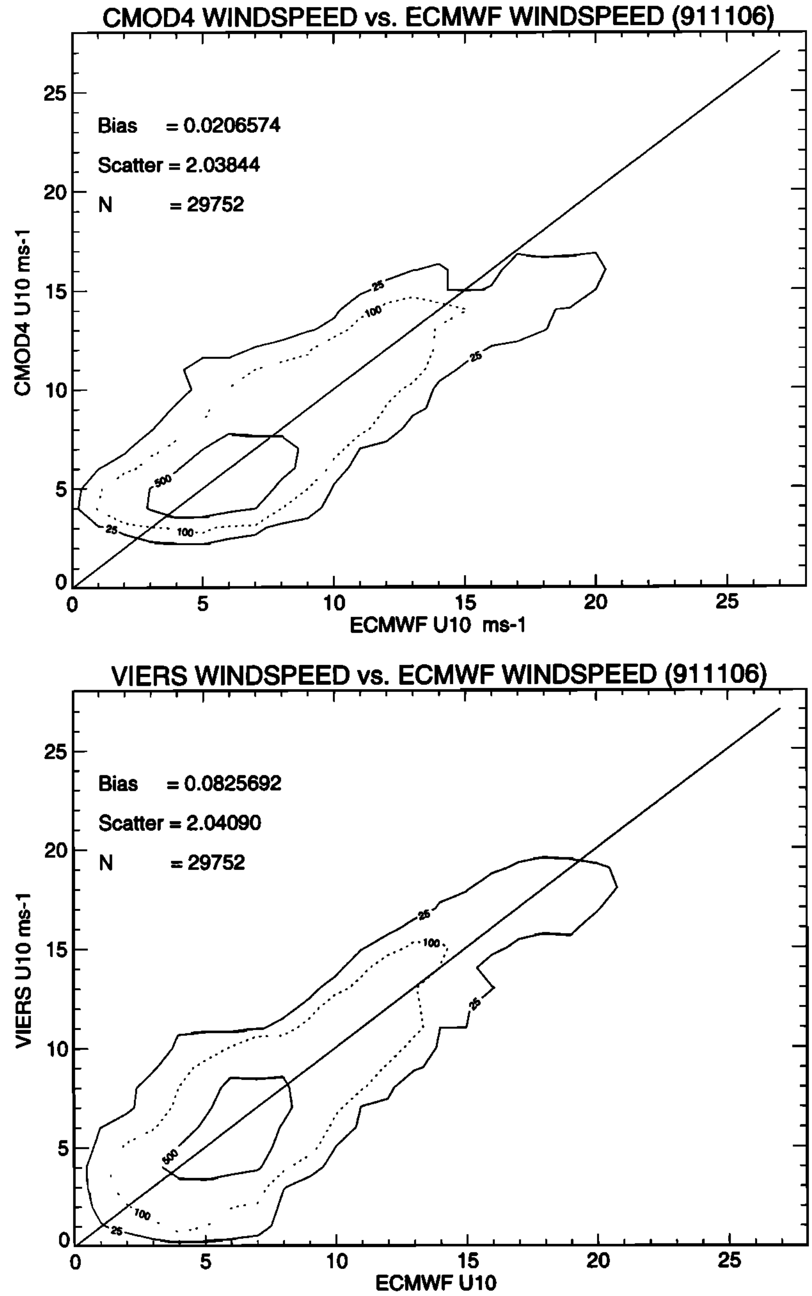

Figure 6. Retrieved wind speed using (top) CMOD4 and (bottom) VIERS algorithm versus analyzed ECMWF wind speed on November 6, 1991.

4.1. Statistical Comparison

We have applied the wind retrieval algorithms of VIERS and CMOD4 to three cases on November 6 and 7, 1991, and March 10, 1992, all on 1200 UT. To that end we collocated the σ_0 triplets, as measured by the ERS-1 scatterometer with wave periods of the WAM model and with analyzed wind fields from the ECMWF atmospheric model.

As a first result, we compare retrieved wind speed and direction from VIERS with the analyzed ECMWF winds. The comparison for the three dates is shown in Figures 6–11. As a reference, the same plots are produced with CMOD4 using the same inversion technique as VIERS. As already discussed, we have performed fine tuning of the VIERS algorithm on the November 6 case. The results of the two other dates show that the tuning procedure was robust. Although the standard deviation of error on these last two dates has increased somewhat, it should be noted that for CMOD4 a similar remark applies.

Statistical parameters for the three dates are summarized in Table 1. Regarding the wind vector, the statistics of VIERS and CMOD4 are comparable, with VIERS having slightly better directional properties. However, as may be inferred from Figures 6, 8, and 10, CMOD4 does not allow wind speeds below 2 m/s, and this may contribute to more favorable statistics. Furthermore, CMOD4 seems to underestimate the wind speed for high winds. In order to see this point more clearly we have restricted the determination of the statistical parameters to those cases where the analyzed ECMWF wind was higher than 15 m/s. Results are given in Table 2.

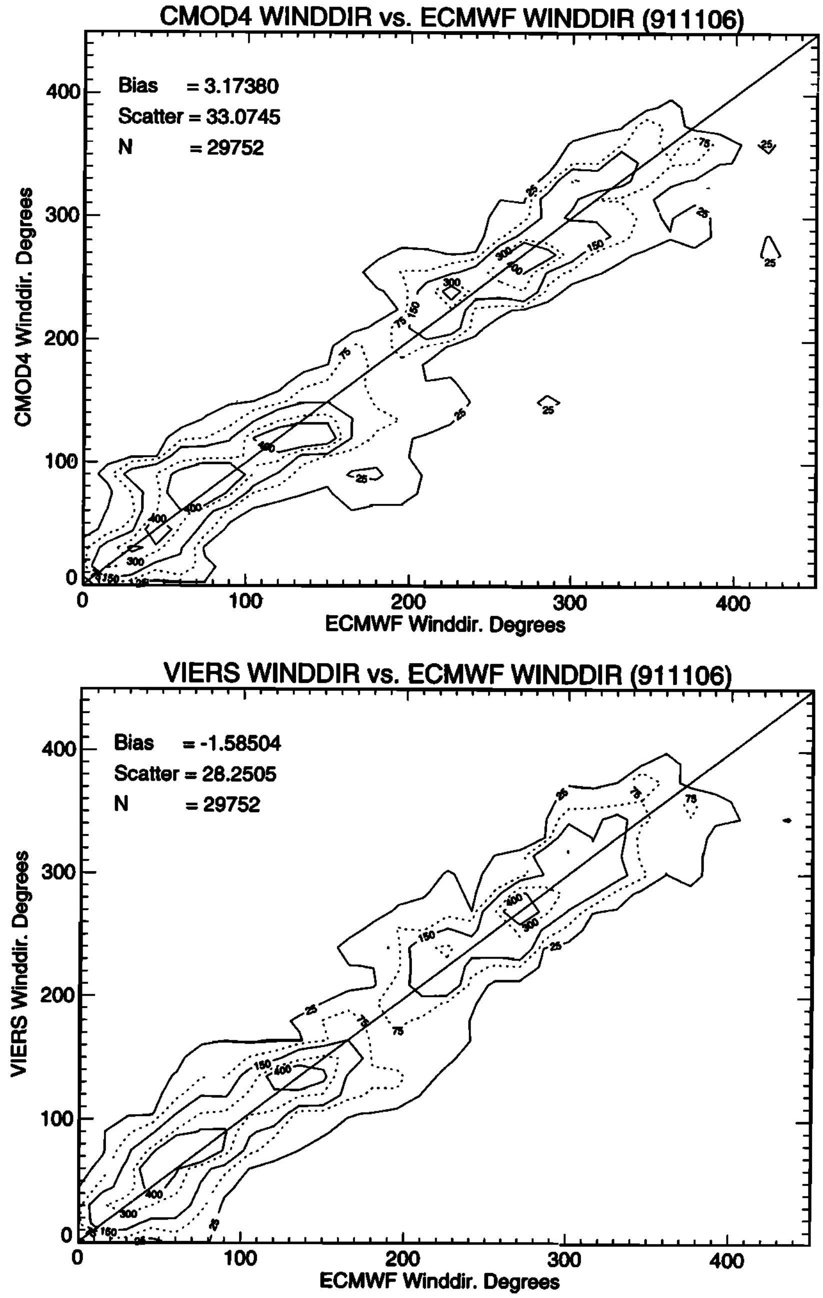

Figure 7. Same as Figure 6, but for wind direction.

The statistics in Table 2 show that both retrieval algorithms are biased low but that CMOD4 clearly underestimates the wind speed. It is emphasized that an underestimation of wind speed at high winds is an undesirable property of a retrieval algorithm. As shown by *Gaffard and Roquet* [1995], when used in an atmospheric data assimilation scheme, the retrieved winds could result in a considerable slowing down of the major storm systems. Of course, our conclusion on the weak performance of CMOD4 at high winds depends on the quality of the analyzed ECMWF winds. However, *Gaffard and Roquet* [1995] also compared CMOD4 wind speeds with quality-controlled buoy wind measurements over a 2-year period. The data set was provided by Météo-France and consisted of buoy reports received through the Global Telecommunications System, which are closer than 100 km in space and 3 hours in time to scatterometer measurements. CMOD4 was found to overestimate wind speeds in the low wind speed range by about 1 m/s, while in the high wind speed range, CMOD4 underestimated wind speed by as much as 2 m/s or even larger. On the basis of the comparison between CMOD4 and the buoy observations, *Gaffard and Roquet* [1995] applied a wind speed dependent bias correction to the wind speeds retrieved by CMOD4, and, in comparison with the ECMWF first-guess winds, hardly any bias was found in the wind speed range up to 20 m/s. When the corrected CMOD4 winds were used in ECMWF's analysis system, an improved agreement between radar altimeter wind speeds and analyzed wind speed was found, while also the forecast showed improvements.

It is therefore concluded that for high wind speeds the VIERS algorithm performs better than CMOD4. A similar re-

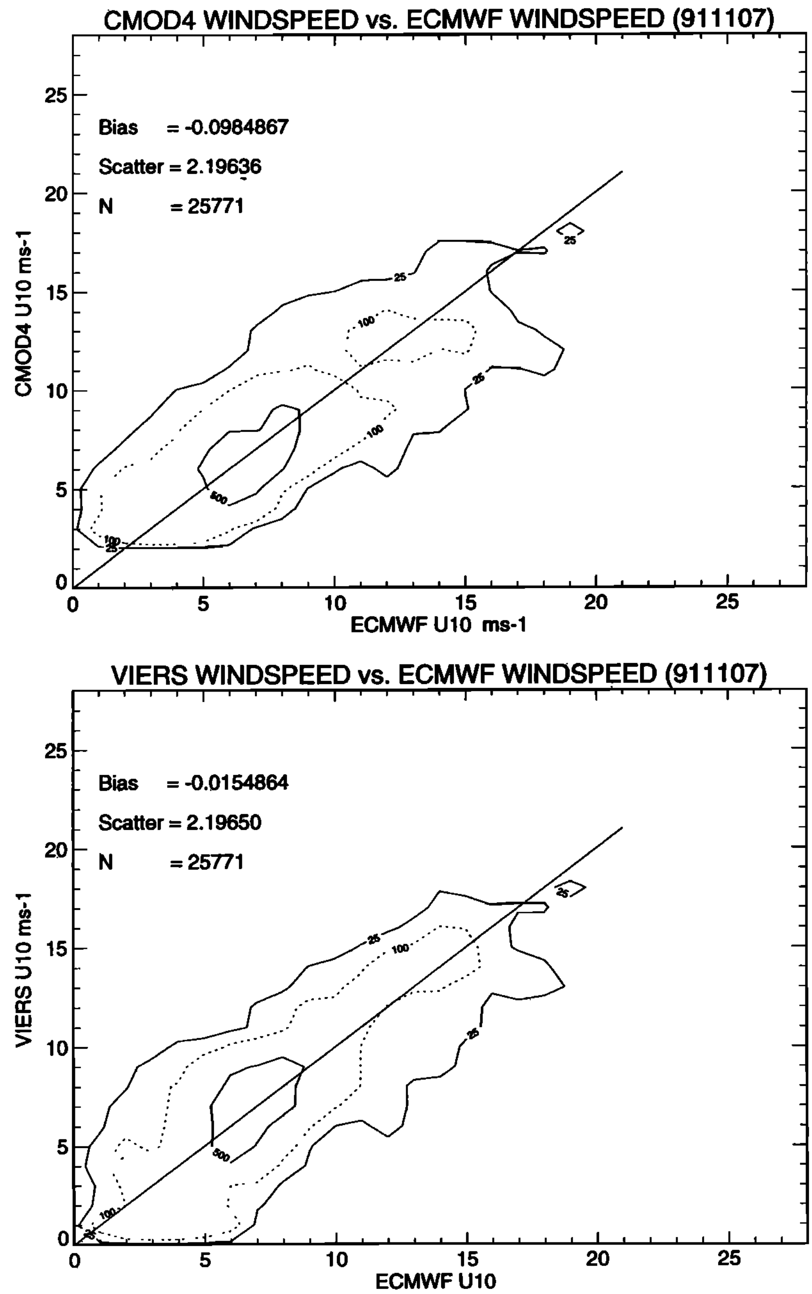

Figure 8. Same as Figure 6, but for November 7, 1991.

mark applies to the low wind speed cases. A summary of the difference in wind retrieval of VIERS and CMOD4 is given in Figure 12. The differences at low and high wind speed confirm the picture we have sketched above. Finally, H. Roquet (private communication, 1995) compared retrieved VIERS winds with the buoy data and found a good agreement, in particular at high wind speeds.

It is emphasized that high wind cases usually correspond to young wind sea because the timescale to reach equilibrium condition is proportional to wind speed. One of the reasons to develop the VIERS algorithm was that it was expected that the radar backscatter depends on the sea state. Young wind waves are usually steeper than old wind waves, and therefore for the same wind speed a larger backscatter would result (compare Figure 3). However, if one would not take the sea state dependence of the radar backscatter into account (by taking, for example, a fixed wave age $c_p/u_* = 35$), then the short waves would be less steep, giving for the same wind a smaller backscatter. As a consequence, with the same observed backscatter one would expect larger winds in a sea state independent algorithm. This turns out to be the case. We reran the VIERS algorithm in sea state independent mode by fixing the wave age c_p/u_* to a constant value, $c_p/u_* = 35$. We took the period of November 6, 1991, and we restricted the wind retrieval to those cases where the ECMWF wind speed is larger than 15 m/s. When comparing the thus obtained retrieved winds with analyzed winds, we found, as expected, a positive bias of 1.64 m/s while the standard deviation of error was 2.74 m/s, which is considerably larger than obtained from the sea state dependent version of VIERS (compare Table 2). It is concluded from this

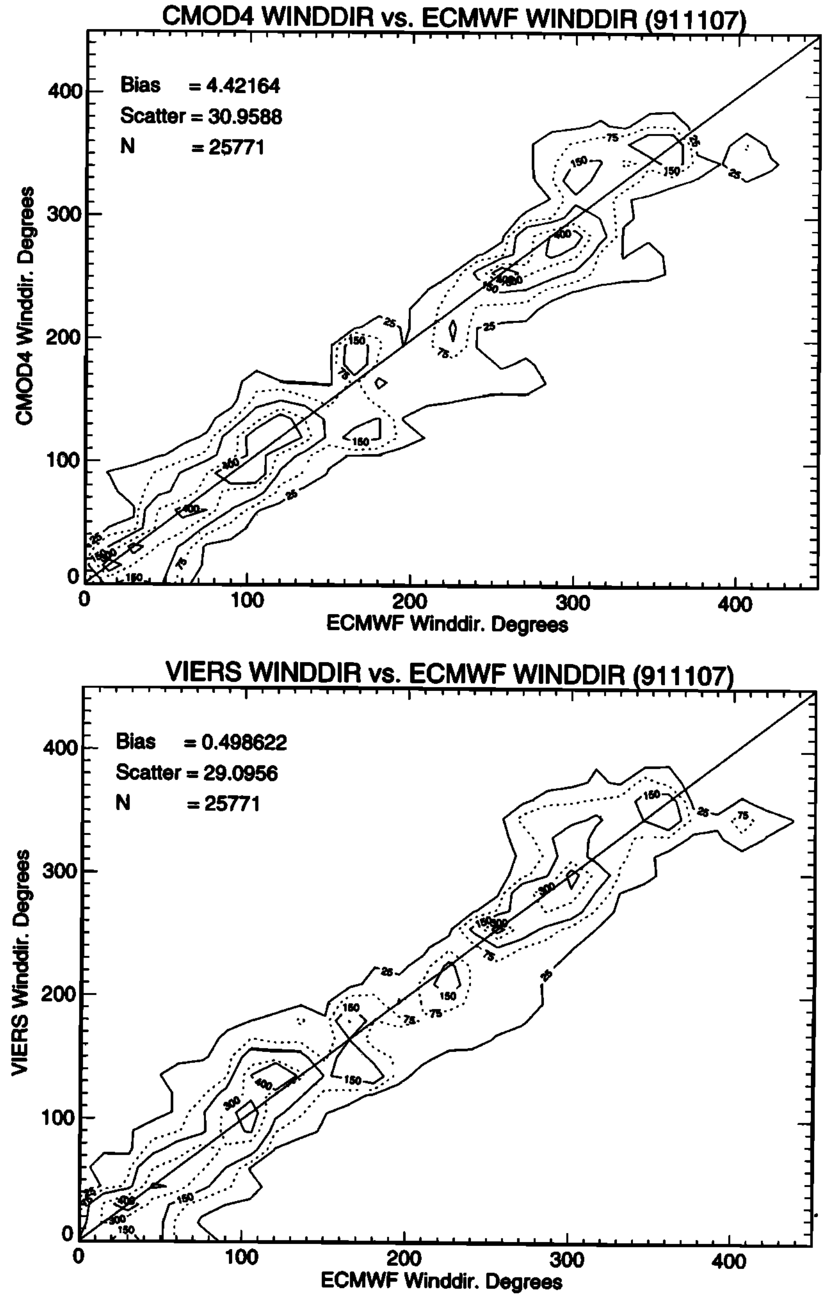

Figure 9. Same as Figure 7, but for November 7, 1991.

comparison that the sea state dependence of radar backscatter has a considerable impact on wind retrieval under a limited range of conditions. It gives rise in a change of bias of 2.5 m/s. Moreover, in view of the smaller standard deviation of error, we conclude that a sea state dependent backscatter algorithm is to be preferred.

In order to finish our discussion on the performance of the VIERS algorithm we finally concentrate on its properties in the so-called σ space. The σ space is the space spanned by the radar backscatter of fore, middle, and aft beam. Let us introduce the distance D_σ in σ space as

$$D_\sigma = \sqrt{Q_{\text{ERS-1}}} \tag{44}$$

where $Q_{\text{ERS-1}}$ is given by (40) then, ideally, a perfect model should have a distance which is as small as possible, i.e., D_σ = 0. There are two reasons why in practice D_σ attains a finite value. The first reason is finite measurement errors. Assuming that there is no bias between model and observation, $\langle\sigma_{\text{obs}} - \sigma_{\text{mod}}\rangle = 0$, and assuming that the backscatter model is perfect, one obtains, using (41),

$$\langle Q_n\rangle = 1$$

and therefore the minimal distance in σ space becomes

$$D_\sigma = \sqrt{3}$$

Assuming, in addition, that the variable $\delta = (\sigma_{\text{obs}} - \sigma_{\text{mod}})/k_p\sigma_{\text{obs}}$ is a Gaussian variable, then for a perfect model the distribution of the distance D_σ can be calculated. Thus the statistics of D_σ are determined by three independent Gaussian

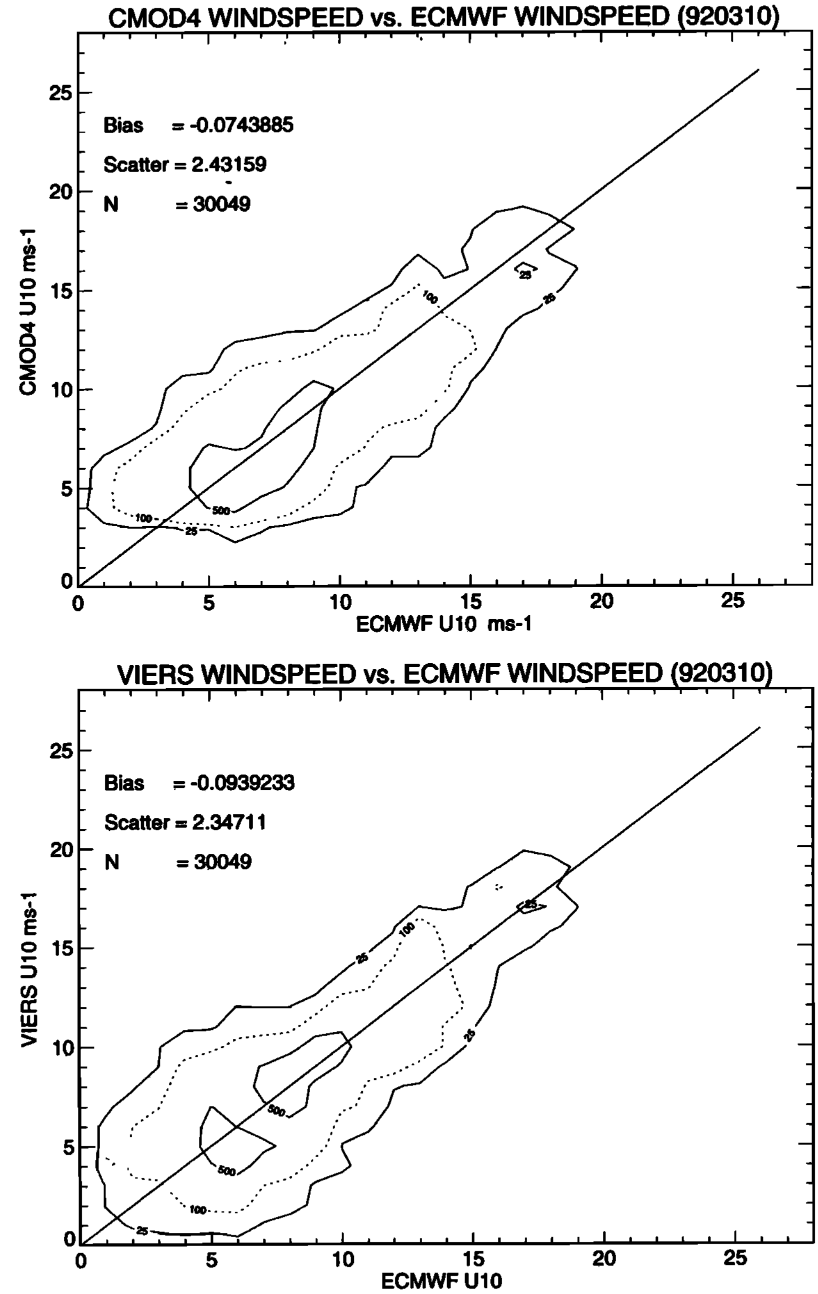

Figure 10. Same as Figure 6, but for March 10, 1992.

variables δ_f, δ_m, and δ_a with $\langle\delta\rangle = 0$ and $\langle\delta^2\rangle = 1$. In that event the distribution of D_σ^2 is chi-square with 3 degrees of freedom. This result is valid if the assumption of independent Gaussian variables is justified and if the model at hand is perfect.

In practice, the actual distribution may deviate from the theoretical one, however. The discrepancy is caused by random model errors (assuming that all systematic errors have been eliminated) that broaden the distribution of δ. As a result, in practice, the mean distance $\langle D_\sigma\rangle$ may be larger than $\sqrt{3}$, and the distribution of D_σ^2 may be different from the chi-square distribution. In Tables 1 and 2 we show the mean values of D_σ for VIERS and CMOD4, and evidently, CMOD4 fits the observed backscatter more closely. This conclusion is supported by Figure 13, where we have plotted the distribution of D_σ for CMOD4 and the VIERS model. The period was November 6, 1991. The distribution for a perfect model is shown as well. We note from Figure 13 that CMOD4 has a more narrow distribution than VIERS, but both model distributions deviate considerably from the one of a perfect model.

Assuming that the model function describes reality in a reasonable manner, it is even possible to infer the rms error of the retrieved wind speed from the misfit in σ space. Of course, a misfit in σ space will induce an error in both wind speed and direction. It is known, however, that the mean of the backscatter from fore and aft beam

$$x = \tfrac{1}{2}(\sigma_a + \sigma_f)$$

is to a good approximation independent of the azimuth angle. This readily follows, assuming Bragg scattering, from the di-

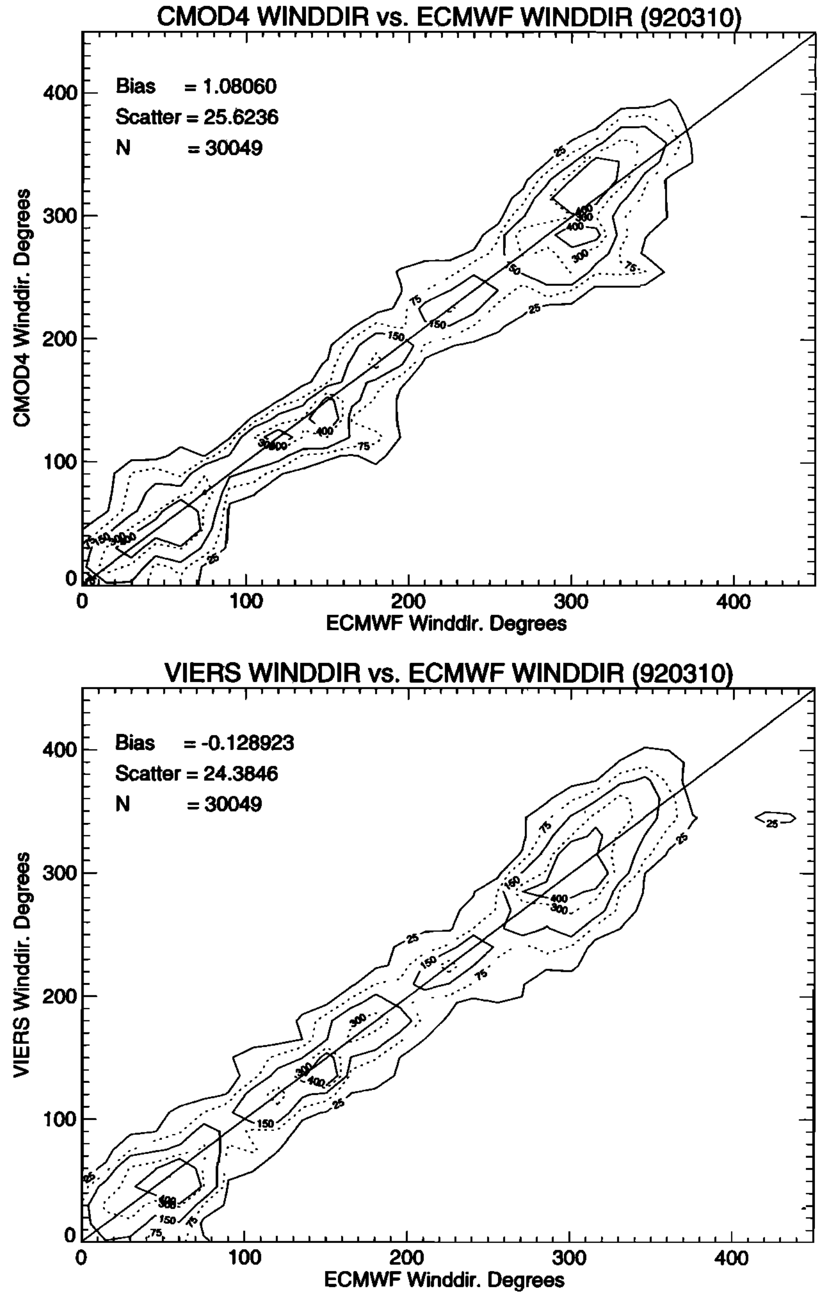

Figure 11. Same as Figure 7, but for March 10, 1992.

rectional wave spectrum, given by (27), which involves a $\cos(2\theta)$, where θ is the difference between azimuth angle and wind angle. Since the azimuth angle for the fore and aft beam is 90° apart, it follows that the sum of fore and aft beam backscatter is independent of azimuth angle. The error in wind speed then immediately follows from

$$\delta x = \frac{\partial x}{\partial U_{10}} \delta U_{10}$$

where δx is the difference between modeled and observed mean backscatter and the derivative of x with respect to U_{10} can be obtained at the minimum distance D by finite differencing. By averaging the square of the error δU_{10} over all retrievals, the overall rms error in wind speed σ_R may be determined according to

$$\sigma_R = \sqrt{\langle \delta U_{10}^2 \rangle}$$

Results of this calculation are shown in Tables 1 and 2. According to this estimate, VIERS has an rms error in wind speed of about 0.75 m/s, and CMOD4 has an rms error of 0.5 m/s, while for the high wind speed cases of Table 2 we get 1 m/s and 0.6 m/s, respectively.

All in all, it is difficult to decide which algorithm is better. On the one hand, CMOD4 has a smaller rms error in wind speed because the misfit in σ space is smaller than for VIERS. On the other hand, when compared to buoy observations and ECMWF analyses, CMOD4 underestimates wind speed considerably while VIERS has less problems in that respect. We therefore conclude that the VIERS model is an acceptable model to retrieve the wind vector from radar backscatter measurements.

Table 1. Statistical Comparison of VIERS and CMOD4 Winds Against ECMWF Analyzed Winds

	November 6, 1991		November 7, 1991		March 10, 1992	
	VIERS	CMOD4	VIERS	CMOD4	VIERS	CMOD4
Number	29752	29752	25771	25771	30049	30049
μ_u, m/s	−0.08	−0.02	0.02	0.10	0.10	0.07
σ_u, m/s	2.04	2.04	2.20	2.20	2.35	2.43
μ_ϕ, deg	1.6	−3.2	−0.5	−4.4	0	−1
σ_ϕ, deg	28	33	29	31	24	26
D_σ	5.2	3.8	5.9	3.9	5.4	3.7
σ_R, m/s	0.75	0.47	0.80	0.47	0.69	0.49

Here, μ refers to the bias and σ is the standard deviation. Also, the distance between modeled and observed backscatter is given, as well as the anticipated error in wind speed caused by the misfit in σ_0 space.

Although the VIERS model seems to perform in a reasonable manner, it is still of interest to discuss possible reasons for the larger misfit in σ space. An important factor could be the choice of the directional distribution of waves. In VIERS (compare (26)) we use a rather simple direction spectrum with a friction velocity dependent width. From observations it is known that the width also depends on the ratio of wave number to peak wave number of the spectrum [*Donelan et al.*, 1985]. In addition, *Jähne and Riemer* [1990] have observational evidence for a bimodal distribution. In order to see to what extent the directional distribution of the waves plays a role in the wind retrieval, it was decided to do a retrieval experiment using only the fore and aft beam, since the mean of fore and aft beam backscatter is approximately independent of the directional distribution. A much better fit of the VIERS model to the observed backscatter was obtained in this manner. The resulting wind speed error obtained from the misfit in σ space now becomes only 0.5 m/s. Since a retrieval with three beams gives a larger rms error of 75 cm/s, this suggests that our choice of directional distribution of the waves is not optimal. After the VIERS project was finished, *Janssen and Wallbrink* [1997] improved the directional distribution and were able to obtain a misfit in σ space that was similar to the one of the CMOD4 algorithm, but the quality of the wind retrieval product remained the same.

4.2. Synoptic Validation Using Cal/Val Data

In this section we shall discuss in some detail results of another method of validating the retrieved wind fields obtained with the VIERS model; namely, we compare wind fields from VIERS with those of a meteorological model and CMOD4. Although this synoptic validation is only qualitative, it has a certain number of advantages over a statistical validation.

1. One can easily verify by eye the internal consistency of the wind speed and directions of adjacent scatterometer cells; in addition, it is fairly straightforward to identify ambiguity errors and incidence angle dependent problems in the algorithm.

2. One can directly compare the structure of the wind fields of ERS-1 derived wind fields and model derived wind fields.

4.2.1. Calibration and validation campaign. When the European Space Agency (ESA) distributed an announcement of opportunity for the calibration and validation of the sensors and products of ERS-1, the VIERS group submitted a proposal for the validation of the wind scatterometer product. This proposal was granted by ESA and access was given to the calibration and validation data acquired during the Cal/Val campaign in the Norwegian part of the North Sea and the Atlantic Ocean between 5°W and 10°E and 60° and 70°N in 1991. ESA was the initiator of this large campaign in which information on the ocean and weather conditions was acquired during overpasses of the ERS-1 satellite. At that time the satellite was in a 3-day repeat period orbit, which had a scatterometer crossover point west of Norway.

The data acquired from the in situ sensors and other sensors were used together with those of the Norwegian meteorological model (hereinafter referred to as METEO) to provide the best possible estimate of the wind field over the scatterometer swath during the passage of the satellite. Besides the ERS-1 measured triplets of the radar scattering at the ocean surface the VIERS model needs to have the peak frequency of the

Table 2. Same as Table 1, but Under the Restriction of ECMWF Wind Speed Faster Than 15 m/s

	November 6, 1991		November 7, 1991		March 10, 1992	
	VIERS	CMOD4	VIERS	CMOD4	VIERS	CMOD4
Number	1324	1324	1124	1124	1237	1237
μ_u, m/s	−0.89	−2.56	−2.18	−3.04	−0.14	−1.26
σ_u, m/s	2.02	2.02	2.13	2.51	2.55	2.44
μ_ϕ, deg	−3.2	−4.8	−6.2	−6.8	4.9	4.2
σ_ϕ, deg	12.3	11.5	14.8	15.4	15.5	15.0
D_σ	5.1	3.6	4.5	3.0	4.7	3.6
σ_R, m/s	1.14	0.60	0.84	0.52	0.98	0.71

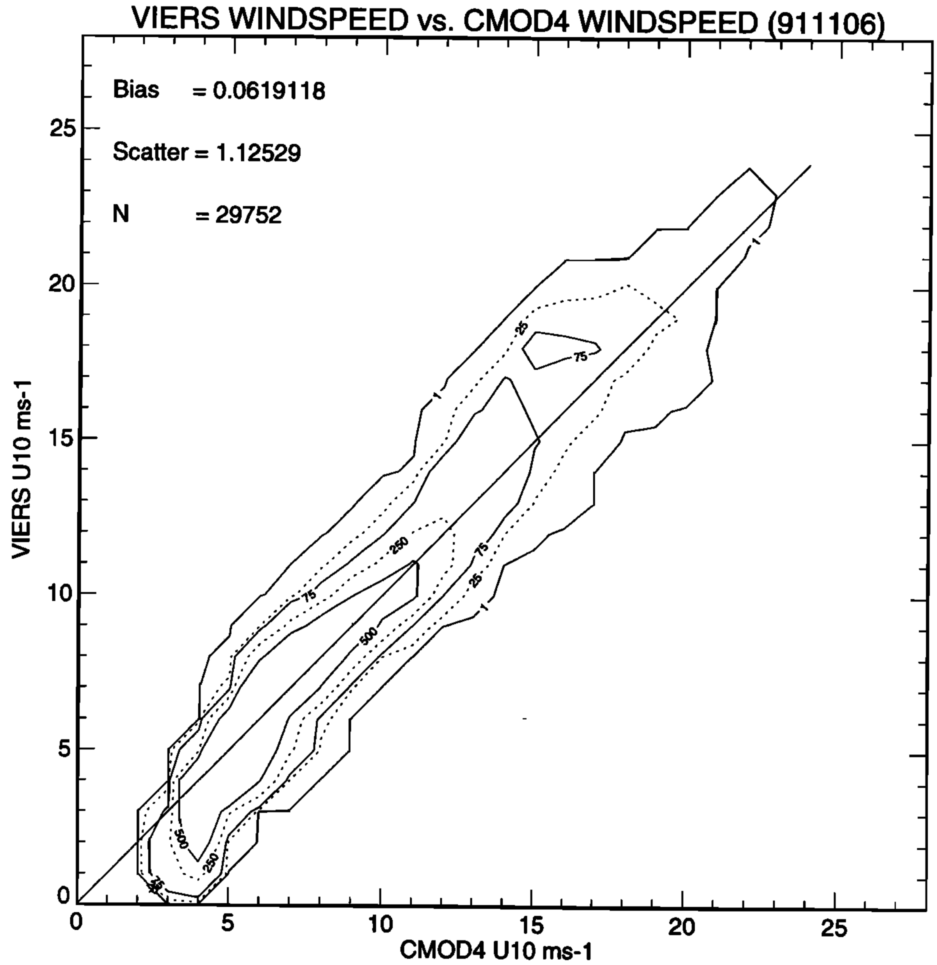

Figure 12. Comparison of VIERS and CMOD4 wind speed for November 6, 1991.

wind sea part of the dominant waves as input. This parameter was obtained from output of the operational WAM model at the Royal Netherlands Meteorological Institute (KNMI), which was kindly provided by J. Onvlee (personal communication, 1993).

Retrieved VIERS winds were then generated by running the inverse VIERS model using the collocated METEO winds as side condition. In a similar fashion, CMOD4 retrieved winds were obtained. The resulting winds were imaged on a plane tangential to the earth at 65°N and 5°E. An example is given in Plate 1. Here wind speed is coded by a color scale, where the scale ranges from 0 to 24 m/s while the arrows in the plot indicate the flow direction.

Table 3 presents an overview of the data used. It lists mean wind speeds and the differences between model and ERS-1 derived winds, as well as the differences between VIERS and CMOD4. Assuming neutral conditions, the average difference between VIERS and METEO is 0.8 m/s, and between CMOD4 and METEO the average difference is 0.3 m/s. The standard deviation of the difference between VIERS and METEO is 2.3 m/s and is 2.0 m/s for CMOD4 and METEO. If unstable conditions are assumed (we took a fixed air-sea temperature difference of −5°K), which is the usual condition for this part of the ocean in the autumn, then the mean difference between VIERS and METEO reduces to 0.1 m/s. The differences between VIERS and CMOD4 are much smaller than between each of them with the METEO winds.

4.2.2. Qualitative analysis. A qualitative analysis was performed on all data which were made available by ESA. This analysis led to a number of conclusions, which were illustrated by four case studies in *Janssen et al.* [1995]. Here we only discuss one case study, namely the detection and localization of fronts, while also the main conclusions are summarized.

We study here briefly a case in which a large front is visible in the ERS-1 data. On the southwestern part of the front the wind direction is southwesterly; on the other side of the front the wind direction is northeasterly. Plate 1 shows the VIERS retrieved wind field on November 6, 1991, in large and the corresponding METEO and CMOD4 wind field in the subimages. When comparing the images, a striking correspondence between the VIERS and CMOD4 result on the one side is seen while there is a clear discrepancy between the METEO winds and the ERS-1 derived winds. In the METEO wind field the front is not as pronounced as in the ERS-1 derived wind fields, and the position is ~200 km north of the front observed by ERS-1.

This example illustrates the conclusion that the ERS-1 derived wind fields show more structure than the meteorological model fields. Furthermore, the difference between VIERS wind fields and CMOD4 wind fields is generally smaller than

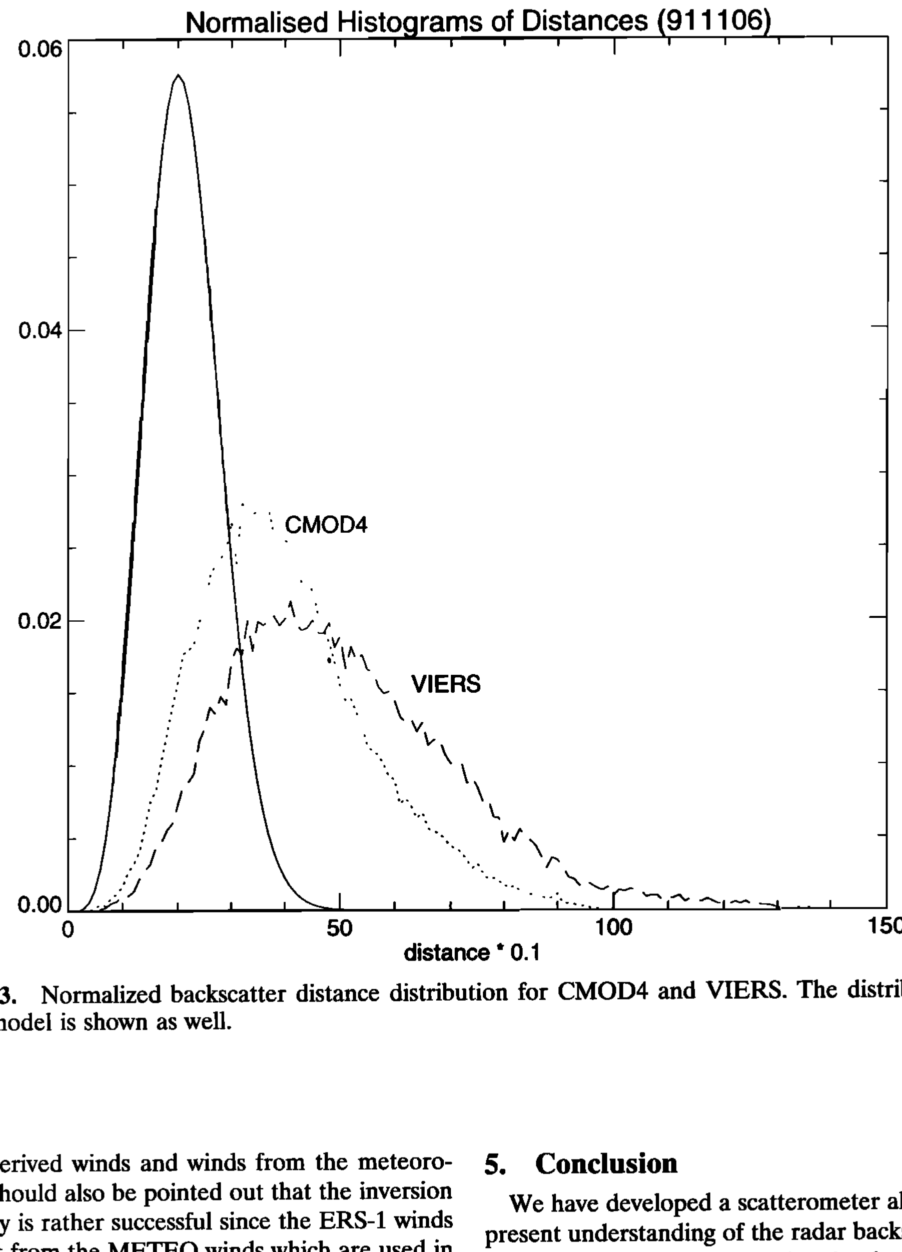

Figure 13. Normalized backscatter distance distribution for CMOD4 and VIERS. The distribution for a perfect model is shown as well.

between ERS-1 derived winds and winds from the meteorological model. It should also be pointed out that the inversion method we employ is rather successful since the ERS-1 winds are quite different from the METEO winds which are used in the minimization of the cost function D. An exception has to be made in case the METEO wind direction is orthogonal to the expected wind direction. In that event the inversion procedure is not always finding the right direction.

Additional observations we have inferred from studying the wind field maps are (1) because at small incidence angles the dependence on wind direction is weak, the retrieved wind direction in cells with these small incidence angles is less reliable; fortunately, this only occurred in the cell with the smallest incidence angle; (2) VIERS wind directions have a better internal consistency than CMOD4 directions; and (3) the VIERS model is capable of dealing with very low wind speeds.

Summarizing, we conclude that the structure of the VIERS wind fields and CMOD4 wind fields is very similar indeed, while the difference between METEO and ERS-1 derived wind fields is bigger. This is probably related to the fact that the METEO wind fields show much less structure than both fields from VIERS and CMOD4. Once more, it may be concluded that the VIERS model is an acceptable algorithm to retrieve the wind vector from radar backscatter measurements.

5. Conclusion

We have developed a scatterometer algorithm based on the present understanding of the radar backscatter process and of the relevant processes governing the short wave spectrum. The final aim was to be able to obtain wind fields from the backscatter as observed by the scatterometer on board of satellites such as ERS-1.

Using observed wave spectra and observed backscatter in the laboratory, it was readily realized that a simple two-scale model for the scattering process performed relatively well. In addition, it turned out that the short wave model was compatible with the wave measurements in the sense that spectra sufficiently close to the measured ones could be generated by tuning parameters which were not fixed a priori. As a final result, the two-scale model was combined with the wave model into the VIERS scatterometer algorithm. After a fine tuning exercise the algorithm evolved into the form described in this paper.

The present VIERS model has been shown to retrieve wind fields in a satisfactory manner; this followed both from the statistical comparison with ECMWF and CMOD4 wind fields and from the synoptic discussions. Furthermore, we have developed a method which enables us to retrieve, in a cost effec-

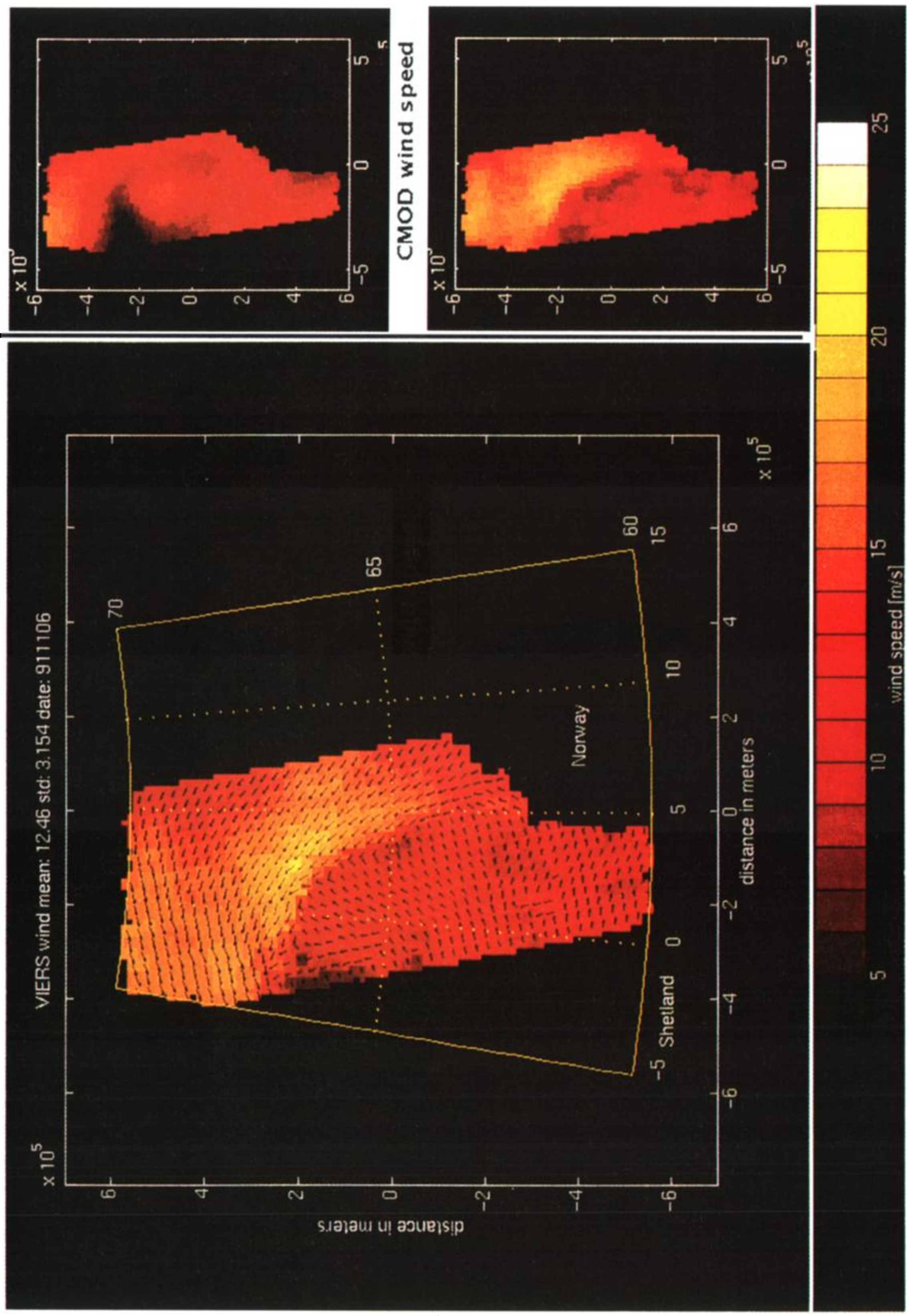

Plate 1. Retrieved wind fields from (left) VIERS, (top right) METEO, and (bottom right) CMOD4 on November 6, 1991. Area is the Norwegian Sea.

Table 3. Comparison of VIERS and CMOD4 Retrieved Winds With Analyzed METEO Winds During Cal/Val Campaign

				VIERS-METEO		CMOD4-METEO		VIERS-CMOD4	
Date	METEO	VIERS (Neutral)	CMOD4	Average	Standard Deviation	Average	Standard Deviation	Average	Standard Deviation
Sept. 19, 1991	11.6	10.1	10.1	−1.5	1.4	−1.4	1.2	−0.1	0.6
Sept. 22, 1991	14.1	9.3	8.6	−4.8	2.4	−5.5	2.5	0.8	0.7
Sept. 28, 1991	5.9	6.0	6.2	0.1	2.0	0.3	1.9	−0.2	0.6
Oct. 7, 1991	10.9	11.1	10.8	0.2	3.3	−0.0	3.1	0.3	0.6
Oct. 10, 1991	7.4	7.3	7.5	−0.2	1.6	0.0	1.5	−0.2	0.5
Oct. 19, 1991	9.9	13.6	12.9	3.7	1.5	3.1	0.9	0.6	0.8
Oct. 22, 1991	9.9	11.5	11.8	1.5	1.6	1.9	1.2	−0.4	0.7
Oct. 28, 1991	5.4	4.9	5.0	−0.5	1.4	−0.4	1.2	−0.1	0.5
Nov. 3, 1991	6.4	7.8	7.8	1.4	3.0	1.4	2.3	0.0	1.1
Nov. 6, 1991	3.1	3.4	4.1	0.3	1.8	0.9	1.7	−0.6	0.7
Nov. 12, 1991	6.5	7.8	8.1	1.3	1.9	1.6	1.8	−0.3	0.6
Nov. 15, 1991	2.0	4.3	4.7	2.3	2.1	2.7	1.7	−0.4	0.8
Nov. 21, 1991	13.2	17.1	15.6	3.8	3.1	2.4	3.0	1.4	1.1
Nov. 24, 1991	11.4	14.6	14.1	3.2	4.3	2.7	4.3	0.5	1.0
Nov. 30, 1991	14.4	14.4	13.6	0.0	2.8	−0.8	2.2	0.8	0.8
Dec. 3, 1991	11.2	13.5	13.2	2.3	1.1	2.0	1.1	0.3	0.6
Dec. 9, 1991	8.9	9.9	10.2	1.0	2.4	1.3	2.1	−0.3	0.7
Sept. 18, 1991	13.2	10.7	10.0	−2.5	3.5	−3.2	3.4	0.7	1.1
Sept. 24, 1991	10.2	10.2	9.1	−0.1	4.0	−1.1	3.8	1.1	1.0
Sept. 27, 1991	5.8	5.9	6.1	0.1	2.8	0.3	2.4	−0.2	1.0
Oct. 3, 1991	11.6	10.5	9.8	−1.1	2.2	−1.8	2.1	0.7	1.4
Oct. 6, 1991	7.7	8.2	7.9	0.5	1.6	0.2	1.1	0.3	1.2
Oct. 12, 1991	4.1	5.5	5.5	1.5	3.0	1.4	2.4	0.0	1.2
Oct. 15, 1991	2.8	2.8	3.7	0.0	1.7	0.9	1.2	−0.9	1.1
Oct. 21, 1991	6.9	9.7	9.5	2.8	1.9	2.6	1.6	0.2	0.9
Oct. 24, 1991	7.3	7.2	7.4	−0.0	1.9	0.1	1.6	−0.2	0.9
Oct. 30, 1991	12.0	6.7	6.6	−5.3	3.3	−5.4	2.7	0.1	1.1
Nov. 2, 1991	8.9	9.1	8.2	0.2	2.0	−0.7	1.5	0.8	1.0
Nov. 8, 1991	8.4	9.3	9.4	1.0	2.2	1.0	1.6	−0.0	1.3
Nov. 11, 1991	11.2	13.4	12.1	2.2	1.9	0.8	1.6	1.4	1.1
Nov. 17, 1991	4.7	7.3	7.1	2.6	2.9	2.5	2.3	0.2	1.2
Nov. 26, 1991	12.0	13.9	12.4	1.8	2.5	0.4	2.0	1.5	1.4
Dec. 2, 1991	12.3	14.9	13.2	2.6	2.0	0.9	1.6	1.7	1.2
Dec. 5, 1991	7.2	7.9	7.9	0.7	1.6	0.7	1.3	0.1	1.0
Sept. 19, 1991	12.5	16.5	14.0	4.0	1.1	1.5	1.3	2.5	1.2
Sept. 22, 1991	5.2	5.7	6.2	0.5	3.9	1.0	3.5	−0.5	1.2
Sept. 28, 1991	5.2	6.1	6.0	0.9	2.2	0.8	1.4	0.1	1.2
Oct. 1, 1991	10.9	12.4	11.4	1.5	1.9	0.5	1.6	1.0	1.2
Oct. 7, 1991	11.2	11.3	10.1	0.1	2.4	−1.1	1.7	1.1	1.3
Oct. 10, 1991	10.1	10.0	9.2	−0.0	1.5	−0.9	1.1	0.9	1.1
Oct. 16, 1991	12.6	13.6	13.3	1.0	2.3	0.7	1.9	0.3	1.1
Oct. 19, 1991	6.8	7.7	7.4	0.9	2.2	0.6	2.0	0.4	1.2
Oct. 25, 1991	8.0	8.3	7.8	0.3	1.5	−0.2	1.0	0.5	1.2
Oct. 28, 1991	8.8	8.3	7.4	−0.4	2.0	−1.4	1.1	0.9	1.3
Nov. 3, 1991	13.0	15.1	13.9	2.1	2.5	0.9	2.1	1.2	1.3
Nov. 6, 1991	10.0	12.5	12.0	2.5	3.6	2.0	3.8	0.4	1.1
Nov. 12, 1991	9.5	10.1	9.3	0.5	2.1	−0.2	1.6	0.8	1.4
Nov. 15, 1991	9.5	11.5	10.2	2.0	2.9	0.7	2.9	1.2	1.3
Nov. 21, 1991	8.5	8.8	8.2	0.3	1.9	−0.3	1.7	0.6	1.1
Nov. 24, 1991	10.4	11.2	10.0	0.8	2.8	−0.4	2.2	1.2	1.2
Nov. 30, 1991	9.0	11.5	10.3	2.5	2.1	1.2	1.9	1.3	1.3
Dec. 3, 1991	8.4	8.2	7.6	−0.2	2.2	−0.8	1.8	0.6	1.1
Statistics				0.8	2.3	0.3	2.0	0.5	1.0
Neutral				0.1	2.4	0.3	2.0	−0.2	1.1
Unstable									

tive way, wind fields using a rather complicated and expensive algorithm such as VIERS. In fact, it has been shown that in an operational environment, retrieval of VIERS winds may be done as efficiently as with the present operational CMOD4 algorithm.

Although the retrieved winds from VIERS and CMOD4 are of comparable quality in a statistical sense, we found that compared to the ECMWF wind fields, the CMOD4 winds are biased low in the high wind speed range. A similar conclusion follows from a comparison with buoy observations. The VIERS bias was much less in this range. It should be once more emphasized that a reliable retrieval of winds in the high wind speed range is important. A negative bias in the wind retrieval would result in a considerably less deep analyzed depression since over the oceans the wind vector is related to a good approximation to the pressure gradient (geostrophic balance).

A weak point of the VIERS algorithm is the too simple directional distribution of the short waves. This is probably the major cause of the larger misfit in σ space (when compared to CMOD4). The strong point of the VIERS algorithm, on the other hand, is that we have followed an approach based on physics. The framework of physical modeling as given by VIERS offers great potential for the future. Although CMOD4 at the moment shows a closer fit between modeled and observed backscatter, new insights into the directional distribution of the short waves will improve the performance of VIERS in this respect. Because of our framework this is a relatively easy step to take. In addition, in this way we were able to incorporate effects of sea state, slicks, and atmospheric stability in a natural manner. Finally, the VIERS algorithm has the added advantage that it can be applied to a fairly wide range of radar frequencies; hence without too much tuning one would expect that it should do a reasonable job of wind retrieval from backscatter from other scatterometers.

Acknowledgments. Useful discussions with David Anderson, Tony Hollingsworth, Ad Stoffelen, and Pete Woiceshyn are much appreciated. We thank J. Onvlee for providing WAM model data during the Cal/Val campaign. This work was supported by the Netherlands Remote Sensing Board (BCRS).

References

Alpers, W., and H. Hühnerfuss, The damping of ocean waves by surface films: A new look at an old problem, *J. Geophys. Res.*, *94*, 6251–6265, 1989.

Anderson, D., A. Hollingsworth, S. Uppala, and P. Woiceshyn, A study on the feasibility of using sea and wind information from the ERS-1 satellite, ESA report, part 1, 121 pp., Eur. Cent. for Medium-Range Weather Forecasts, Reading, England, 1987.

Andersson, E., et al., The ECMWF implementation of three-dimensional variational assimilation (3D-Var), III, Experimental results, *Q. J. R. Meteorol. Soc.*, in press, 1998.

Apel, J. R., An improved model of the ocean surface wave vector spectrum and its effects on radar backscatter, *J. Geophys. Res.*, *99*, 16,269–16,291, 1994.

Bahar, E., D. E. Barrick, and M. A. Fitzwater, Computations of scattering cross sections for composite surfaces and the specification of the wave number where spectral splitting occurs, *IEEE Trans. Antennas Propag.*, *31*, 698–709, 1983.

Banner, M. L., Equilibrium spectra of wind waves, *J. Phys. Oceanogr.*, *20*, 966–984, 1990.

Barrick, D. E., and C. T. Swift, The Seasat microwave instruments in historical perspective, *IEEE J. Oceanic Eng.*, *OE-5*(2), 74–79, 1980.

Brown, G. S., Backscattering from a Gaussian distributed perfectly conducting rough surface, *IEEE Trans. Antennas Propag.*, *26*, 472–482, 1978.

Businger, J. A., J. C. Wyngaard, I. Izumi, and E. F. Bradley, Flux-profile relationships in the atmospheric surface layer, *J. Atmos. Sci.*, *28*, 181–189, 1971.

Calkoen, C. J., et al., Viers-1 progress report, 2, *Tech. Rep. BCRS 90-27*, Neth. Remote Sens. Board, The Hague, 1990.

Davidson, R. C., *Methods in Nonlinear Plasma Theory*, Academic, San Diego, Calif., 1972.

Donelan, M. A., and W. J. Pierson, Radar scattering and equilibrium ranges in wind-generated waves with application to scatterometry, *J. Geophys. Res.*, *92*, 4971–5029, 1987.

Donelan, M. A., J. Hamilon, and W. H. Hui, Directional spectra of wind-generated waves, *Philos. Trans. R. Soc. London A*, *315*, 509–562, 1985.

Dyer, A. J., and B. B. Hicks, Flux-gradient relationships in the constant flux layer, *Q. J. R. Meteorol. Soc.*, *96*, 715–721, 1970.

Gaffard, C., and H. Roquet, Impact of the ERS-1 scatterometer wind data on the ECMWF 3D-Var assimilation system, *ECMWF Tech. Memo. 217*, Eur. Cent. for Medium-Range Weather Forecasts, Reading, England, 1995.

Guinard, N. W., J. T. Ransone Jr., and J. C. Daley, Variation of the NCRS of the sea with increasing roughness, *J. Geophys. Res.*, *76*, 1525–1538, 1971.

Günther, H., A parametric surface wave model and the statistics of the prediction parameters, Ph.D. thesis, 90 pp., Univ. of Hamburg, Hamburg, Germany, 1981.

Hasselmann, K., On the non-linear energy transfer in a gravity wave spectrum, 1, *J. Fluid Mech.*, *12*, 481–500, 1962.

Hasselmann, K., et al., Measurements of wind-wave growth and swell decay during the Joint North Sea Wave Project (JONSWAP), *Dtsch Hydrogr. Z.*, *A8*(12), suppl. 1–95, 1973.

Jähne, B., and K. S. Riemer, Two-dimensional wave number spectra of small-scale water surface waves, *J. Geophys. Res.*, *95*, 11,531–11,546, 1990.

Janssen, J. A. M., and H. Wallbrink, SATVIEW: A semi-physical scatterometer algorithm, *KNMI Sci. Rep. WR 97-03*, R. Neth. Meteorol. Inst., De Bilt, Netherlands, 1997.

Janssen, P. A. E. M., The initial evolution of gravity-capillary waves, *J. Fluid Mech.*, *184*, 581–597, 1987.

Janssen, P. A. E. M., P. Lionello, and L. Zambresky, On the interaction of wind and waves, *Philos. Trans. R. Soc. London A*, *329*, 289–301, 1989.

Janssen, P. A. E. M., C. J. Calkoen, D. van Halsema, W. A. Oost, P. Snoeij, and H. Wallbrink, VIERS-1 final report phase 4, report, Neth. Remote Sens. Board, The Hague, 1995.

Janssen, P. A. E. M., B. Hansen, and J. Bidlot, Verification of the ECMWF wave forecasting system against buoy and altimeter data, *Weather Forecasting*, *12*(4), 763–784, 1997.

Jones, W. L., L. C. Schroeder, and J. L. Mitchell, Aircraft measurements of the microwave scattering signature of the ocean, *IEEE Trans. Antennas Propag.*, *AP-23*, 52–61, 1977.

Jones, W. L., L. C. Schroeder, D. H. Boggs, E. M. Bracalente, R. A. Brown, G. J. Dome, W. J. Pierson, and F. J. Wentz, The Seasat-A satellite scatterometer: The geophysical evaluation of remotely sensed wind vectors over the ocean, *J. Geophys. Res.*, *87*, 3297–3317, 1982.

Kitaigorodskii, S. A., On the theory of the equilibrium range in the spectrum of wind-generated gravity waves, *J. Phys. Oceanogr.*, *13*, 816–827, 1983.

Klinke, J., and B. Jähne, 2D wave number spectra of short wind waves: Results from wind-wave facilities and extrapolation to the ocean, paper presented at the Conference on Optics of the Air-Sea Interface, Theory and Measurements, Int. Soc. for Opt. Eng., San Diego, Calif., 1992.

Komen, G. J., K. Hasselmann, and S. Hasselmann, On the existence of a fully developed wind-sea spectrum, *J. Phys. Oceanogr.*, *14*, 1271–1285, 1984.

Komen, G. J., L. Cavaleri, M. Donelan, K. Hasselmann, S. Hasselmann, and P. A. E. M. Janssen, *Dynamics and Modelling of Ocean Waves*, 532 pp., Cambridge Univ. Press, New York, 1994.

Lamb, H., *Hydrodynamics*, 6th ed., 738 pp., Dover, Mineola, N. Y., 1932.

Lombardini, P. P., Maximum of damping ratio in rippled water covered by monomolecular films, ONRL report on the role of surfactant films on the interface properties of the sea surface, *Rep. C-11-86*, edited by F. L. Herr and J. Williams, pp. 157–173, Off. of Nav. Res., London, 1986.

Moore, R. J., and A. K. Fung, Radar determination of winds at sea, *Proc. IEEE*, *67*, 1504–1521, 1979.

Moore, R. J., and W. J. Pierson, Measuring sea state and estimating surface winds from a polar orbiting satellite, in *Proceedings of the Symposium on Electromagnetic Sensing of the Earth From Satellites*, edited by R. Zirkland, pp. R1–R28, Polytechnic, New York, 1967.

Phillips, O. M., Spectral and statistical properties of the equilibrium range in wind-generated gravity waves, *J. Fluid Mech.*, *156*, 505–531, 1985.

Plant, W. J., On the steady state energy balance of short gravity wave systems, *J. Phys. Oceanogr.*, *10*, 1340–1352, 1980.

Plant, W. J., Bragg scattering of electromagnetic waves from the air/sea interface, in *Surface Waves and Fluxes*, vol. II, edited by G. L. Geernaert and W. L. Plant, pp. 41–108, Kluwer Acad., Norwell, Mass., 1990.

Schroeder, L. C., D. H. Boggs, G. Dome, I. M. Halberstam, W. L. Jones, W. J. Pierson, and F. J. Wentz, The relationship between wind vector and normalized radar cross section used to derive Seasat-A satellite scatterometer winds, *J. Geophys. Res.*, *87*, 3318–3336, 1982.

Smith, S. D., et al., Sea surface wind stress and drag coefficients: The HEXOS results, *Boundary Layer Meteorol.*, *60*, 109–142, 1992.

Snoeij, P., E. van Halsema, J. Vogelzang, S. Waas, S. Zecchetto, H. Janssen, W. Oost, B. Jähne, and C. Calkoen, VIERS-1 final

report phase 3, *BCRS Rep. 92-24*, Neth. Remote Sens. Board, The Hague, 1993.
Stewart, R. H., *Methods of Satellite Oceanography*, 360 pp., Univ. of Calif. Press, Berkeley, 1985.
Stoffelen, A., and D. Anderson, Scatterometer data interpretation: Estimation and validation of the transfer function CMOD4, *J. Geophys. Res.*, *102*, 5767–5780, 1997.
Valenzuela, G. R., Theories for the interaction of electromagnetic and oceanic waves: A review, *Boundary Layer Meteorol.*, *13*, 612–685, 1978.
Valenzuela, G. R., M. B. Laing, and J. C. Daley, Ocean spectra for the high-frequency waves as determined from airborne radar measurements, *J. Mar. Res.*, *29*, 69–84, 1971.
van Gastel, K., Nonlinear interactions of gravity-capillary waves: Lagrangian theory and effects on the spectrum, *J. Fluid Mech.*, *182*, 499–523, 1987.
van Halsema, D., et al., Progress report on the VIERS-1 project, *Tech. Rep. BCRS 89-24*, Neth. Remote Sens. Board, The Hague, 1989.
Wentz, F. J., S. Peteherych, and L. A. Thomas, A model function for ocean radar cross sections at 14.6 GHz, *J. Geophys. Res.*, *89*, 3689–3704, 1984.
Woiceshyn, P. M., M. G. Wurtele, D. H. Boggs, L. F. McGoldrick, and S. Peteherych, The necessity for a new parameterization of an empirical model for wind/ocean scatterometry, *J. Geophys. Res.*, *91*, 2273–2288, 1986.

C. J. Calkoen, Argoss, Postbus 61, 8325 ZH Vollenhove, Netherlands. (e-mail: Charles.Calkoen@argoss.nl)
P. A. E. M. Janssen, ECMWF, Shinfield Park, Reading RG2 9AX, England, U.K. (e-mail: janssen@ecmwf.int)
W. A. Oost and H. Wallbrink, KNMI, Postbus 201, 3730 AE De Bilt, Netherlands. (e-mail: oost@knmi.nl; wallbrin@knmi.nl)
P. Snoeij, Delft University of Technology, Faculteit Electrotechniek, Postbus 5031, 2600 GA Delft, Netherlands. (e-mail: P.Snoeij@et.tudelft.nl)
D. van Halsema, TNO, Postbus 96864, 2509 JG Den Haag, Netherlands. (e-mail: erik.van.halsema@fel.tno.nl)

(Received December 10, 1996; revised October 3, 1997; accepted October 10, 1997.)